

IN SITU GROWTH STRESSES IN IRON-PLATINUM  
AND IRON-COPPER ALLOY  
THIN FILMS

by

BIANZHU FU

A THESIS

Submitted in partial fulfillment of the requirements  
for the degree of Master of Science  
in the Department of Materials and Metallurgical Engineering  
in the Graduate School of  
The University of Alabama

TUSCALOOSA, ALABAMA

2010



## ABSTRACT

Intrinsic thin film stress is evitable with the thin film deposition process and plays an important role in tuning the physical properties of thin films. In this thesis, the *in situ* and post growth stress evolution of the Fe-Pt and Fe-Cu alloy system was studied and correlated to the microstructure evolutions. At ambient temperature and constant deposition pressure, the growth stresses of both the Fe-Pt and Fe-Cu alloy were found to be dependent on the compositions and affected by their growth rates. The final intrinsic stress states after growth could be tuned to be either tensile, zero or compressive depending upon composition and deposition rate for similar grain sizes. This is due to the preferential segregation of one species (the more mobile element) to the grain boundaries.

At elevated growth temperatures, the Fe-Pt alloy forms ordered phase while the Fe-Cu alloy forms phase separation. The magnitude of the compressive stress state is reduced as the  $\text{Fe}_{54}\text{Pt}_{46}$  thin film orders *in situ* during growth. The compressive stress relaxation rate is increased with increasing substrate temperature or order parameter. This compressive stress reduction has been rationalized as a reduction of adatom mobility on the surface as Fe and Pt occupy specific lattice sites for  $L1_0$  on each grain. The ordered nature of the grains contributes to additional chemical energy at the boundary which, upon ceasing deposition, significantly increases the stress relaxation rate. In contrary, the growth compressive stress of the  $\text{Fe}_{51}\text{Cu}_{49}$  alloys in the continuous growth regime is increased with substrate temperature. This has been rationalized as the migration of adatoms to thermodynamically preferred surfaces during growth.

## DEDICATION

This thesis is dedicated to everyone who helped me and guided me through the trials and tribulations of creating this manuscript. In particular, my family and close friends who stood by me throughout the time taken to complete this masterpiece.

## ACKNOWLEDGMENTS

I would like to express my sincere gratitude to my advisor, Professor Gregory Thompson, for providing invaluable guidance to research and constant supports to my study. I highly appreciate Prof. Thompson for introducing me to scientific research, giving me a chance to accelerate my research skills. The present research work would, therefore, have never been completed without his proper guidance, regular supervision, and constant encouragement.

I would like to thank Professors Gary Mankey and Nitin Chopra for serving on my thesis supervisory committee. I am grateful to them for their careful and critical reading of my thesis and invaluable suggestions. Their comments and suggestions would not only help to improve my research skill but also would be a great help to have deeper insight in future research.

I would like to thank my colleagues, Karen L. Torres, Robert Morris, Diondra Means, Dr Taisuke Sasaki, Chad Hornbuckle for their cooperation and help in the laboratory activities. I would also like to thank the CAF staff Rich Martens, Johnny Goodwin, and Rob Holler for their training of CAF instruments and their help on my experiments.

There can be no adequate acknowledgement for the loving encouragement I have received from all family members. Without their constant support and inspirations all this would never have been possible.

This work was supported by the National Science Foundation, DMR-0529369, and the Alabama Commission on Higher Education Graduate Research Scholars Program.

## CONTENTS

ABSTRACT .....	ii
DEDICATION .....	iii
ACKNOWLEDGMENTS .....	iv
LIST OF TABLES .....	vii
LIST OF FIGURES .....	viii
1. TECHNICAL BACKGROUND.....	1
1.1. Introduction.....	1
1.2. Thin film intrinsic stress evolution .....	4
1.2.1. Origins of pre-coalescence compressive stress.....	7
1.2.2. Origins of intrinsic tensile stress upon island coalescence .....	7
1.2.3. Origins of post-coalescence compressive stress .....	8
1.3. Kinetic parameters .....	12
1.3.1. The influence of deposition pressure .....	12
1.3.2. The influence of substrate temperature.....	12
1.3.3. The influence of deposition rates.....	13
1.3.4. Other factors.....	14
1.4. Fe-Pt and Fe-Cu thin films.....	14
2. EXPERIMENTAL DETAILS .....	16
2.1. Thin film growth.....	16
2.2. Thin film Stress Measurement.....	17

2.3. Structural Characterization .....	19
2.3.1. Quantification of thickness and composition.....	19
2.3.2. Microstructure analysis .....	19
3. COMPOSITIONAL DEPENDENT STRESS STATES .....	22
3.1. Experiment Results .....	22
3.1.1. The Fe-Pt system.....	22
3.1.2. The Fe-Cu system .....	29
3.2. Discussions .....	35
3.3. Conclusions.....	39
4. STRESS EVOLUTION DURING ORDERING .....	40
4.1. Experimental results.....	40
4.2. Discussions .....	46
4.3. Conclusions.....	49
5. STRESS EVOLUTION DURING PHASE SEPARATION .....	51
5.1. Experimental results and Discussion .....	51
5.2. Conclusions.....	60
6. CONCLUSIONS AND FUTURE WORK .....	61
REFERENCES .....	63
APPENDIX A. thermal and under-layer stress subtraction.....	67
APPENDIX B. Fe-Pt and Fe-Cu phase diagram .....	71

## LIST OF TABLES

3.1 The average residual stress and grain size of Fe-Pt thin films.....	27
3.2 The average residual stress and grain size of Fe-Cu thin films .....	27

## LIST OF FIGURES

1.1 Thin film growth modes.....	3
1.2 Typical Thin film stress evolution .....	6
1.3 Microstructure evolution of Volmer-Weber growth.....	6
1.4 Schematic of atoms flowing into grain boundary during growth .....	11
1.5 Stress evolution of Cu thin films deposited at various pressures.....	11
2.1 The AJA sputtering system.....	18
2.2 The MOS setup .....	18
3.1 Stress evolution of Fe-Pt thin films .....	24
3.2 Stress evolution of Fe <sub>65</sub> Pt <sub>35</sub> at different growth rates .....	24
3.3 XRD profiles of Fe-Pt thin films .....	24
3.4 TEM image and diffraction pattern of Fe <sub>65</sub> Pt <sub>35</sub> thin film.....	25
3.5 AFM images of Fe-Pt thin films .....	25
3.6 Atom Probe reconstruction of Fe-Pt thin films.....	28
3.7 XRD profiles of Fe-Cu thin films .....	31
3.8 TEM image and diffraction pattern of Fe <sub>65</sub> Cu <sub>35</sub> thin film .....	31
3.9 TEM image and diffraction pattern of Fe <sub>50</sub> Cu <sub>50</sub> thin film .....	32
3.10 Stress evolution of Fe-Cu thin films .....	32
3.11 Stress evolution of Fe <sub>50</sub> Cu <sub>50</sub> at different growth rates .....	33
3.12 Atom Probe reconstruction of Fe <sub>50</sub> Cu <sub>50</sub> thin film .....	33

3.13 AFM images of the Fe-Cu thin films .....	34
3.14 Stress relaxation of the Fe-Pt and Fe-Cu thin films .....	34
4.1 Stress evolution of Fe <sub>54</sub> Pt <sub>46</sub> thin film at different temperatures.....	42
4.2 Stress evolution of pure Fe and Pt thin films at different temperatures .....	43
4.3 XRD profiles of Fe <sub>54</sub> Pt <sub>46</sub> , pure Pt and Fe .....	44
4.4 AGM results of Fe <sub>54</sub> Pt <sub>46</sub> thin films .....	45
4.5 Illustrations of atoms movement during ordering.....	50
5.1 Stress evolution of Fe <sub>51</sub> Cu <sub>49</sub> thin film at different temperatures .....	53
5.2 XRD and TEM diffraction pattern of Fe <sub>51</sub> Cu <sub>49</sub> thin film grown at room temperature .....	53
5.3 TEM HAADF images of Fe <sub>51</sub> Cu <sub>49</sub> thin films .....	56
5.4 Illustrations of atom movement during phase separation .....	59
5.5 AFM images of Fe <sub>51</sub> Cu <sub>49</sub> thin films.....	59
A.1 Original stress measurement of Pt .....	69
A.2 The stress of Pt after subtraction.....	70
B.1 Fe-Pt phase diagram.....	72
B.2 Fe-Cu phase diagram.....	73

## CHAPTER 1

### TECHNICAL BACKGROUND

#### 1.1. Introduction

Thin films and thin film based devices are widely used in everyday technologies which include memory disks for computers, semiconductor devices for cell phones, gas sensors in automobiles, wear resistant coatings for cutting tools, and thermal barrier layers in power generating turbines. Thin films can provide desired optical, electrical, chemical, magnetic, mechanical and thermal properties [1].

Thin films are manufactured by a variety of methods including evaporation, sputter deposition, pulsed laser deposition and plasma deposition. Based on the vapor supplying methods, these techniques are generally divided into two categories: physical vapor deposition (PVD) and chemical vapor deposition (CVD). Though having different vapor supplying methods, the way that thin films grows on the substrates are similar each includes the nucleation and growth of the islands and the subsequent coalescence of the islands into a continuous film. Depending upon the relative magnitude of the substrate surface free energy  $\gamma_s$ , the film surface free energy  $\gamma_f$  and the film surface interfacial free energy  $\gamma_i$ , the actual thin film developing microstructures can be different, as shown in Fig 1.1 [2]. These different growth modes are the following:

- (i) Volmer-Weber mode, also called three-dimensional (3D) nucleation and growth mode. It occurs when  $\gamma_s < \gamma_f + \gamma_i$ , or, alternatively, the film does not wet the substrate. The accumulation of individual atoms, called adatoms, will form

discrete nucleus of islands whereupon these islands grow, coalescence and impinge into one another to form the continuous film surface. The thin film will not thicken until the continuous film has formed.

- (ii) Frank-Van Der Merwe mode, also called layer by layer growth mode. When  $\gamma_s > \gamma_f + \gamma_i$ , the film wets the substrate and two dimensional nucleation forms and continuous by a layer-by-layer method. These films grow very smoothly and the thickness of the films will be linear function with deposition rate and time.
- (iii) Stranski-Krastanov mode, a combination of the first two modes. In this case, the films will grow in a layer-by-layer mode for the first few mono-layers and then change to a 3D nucleation growth method because of a change in the interfacial energy associated with the initial few mono-layers.

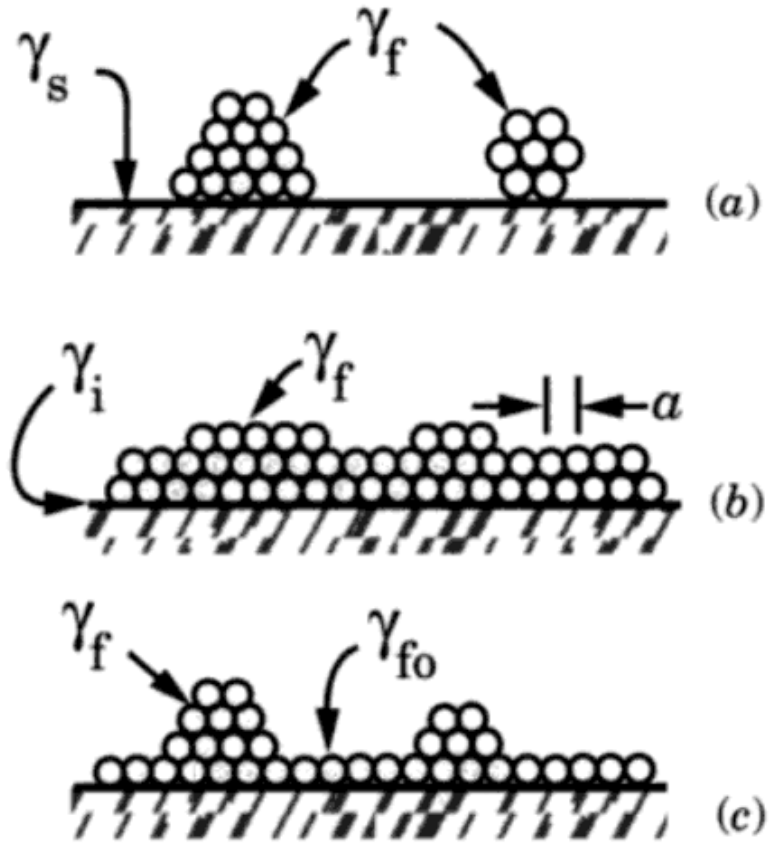


**Figure 1.1:** Film growth modes: (a) Volmer-Weber growth mode, (b) Frank-Van der Merve growth mode, and (c) Stranski-Dransanov growth mode, taken from [2].

Regardless of the thin film growth process, a large stress is usually experienced during the deposition. It is usually higher than the bulk phase modulus and plays an important role in tuning the physical [3-5] and mechanical [6, 7] properties of the thin film. This stress is generally responsible for the failure of the thin film in a device based application. Typical mechanical failures include delamination [7].

In general, the stress observed in thin films can be categorized as the following: (1) misfit stresses, (2) thermal stresses and (3) intrinsic stresses. Misfit stresses arise when the film's bulk lattice spacing being different than that of substrate during in epitaxial (orientation favored) growth. Thermal stresses are generated by a temperature change when the film and the substrate have different thermal expansion coefficients. Intrinsic stresses occur with the microstructure evolution of the thin films, at which the films either expand or shrink if not attached to their substrates [7]. Since the intrinsic stress is directly related to the microstructure evolution, extensive studies have been made on the intrinsic stress evolution of metallic, elemental thin films [7-12].

## 1.2. Thin film intrinsic stress evolution

Most metallic thin films grown on a Si substrate adopt a Volmer-Weber growth mode [7]. In this mode, the thin films generally experience a stress evolution that is dependent on the adatom mobility. For thin films with high adatom mobility like Pt [7], Cu [8], and Ag [9-10], they usually undergo compressive-to-tensile-to-compressive stress evolution. In contrast, thin films with low adatom mobility such as Fe [11], and Co [12], only experience compressive-to-tensile stress changes at room temperature, as shown in Figure 1.2.

The stress evolution of thin films, as stated above, is directly related to the microstructure evolution. For high adatom mobility thin films, it is widely accepted that the initial compressive

stress corresponds to discrete island nucleation; the tensile stress is the coalescence of islands; and the compressive stress after maximum tensile stress comes from the continuous thin film growth after the impingement of islands, as shown in Figure 1.3. For low adatom mobility thin films, the stress does not change after the coalescence of discrete islands.

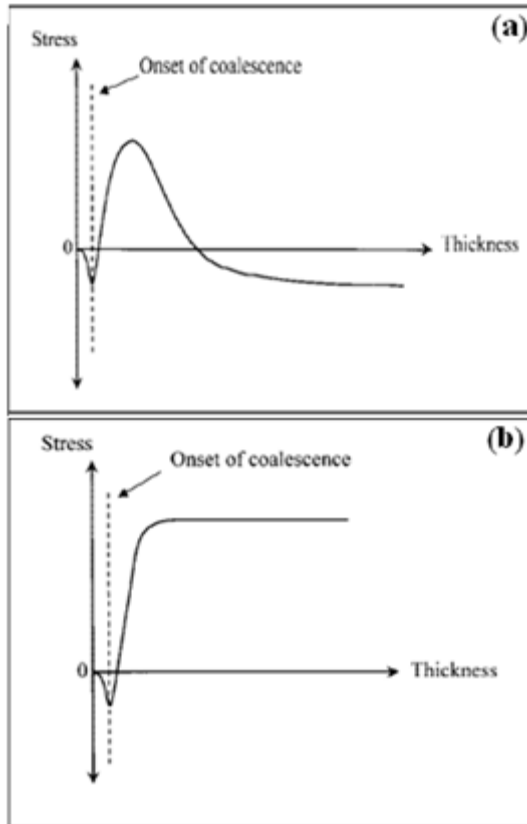


**Figure 1.2:** Schematic illustration of thin film stress evolution versus thickness plot for metallic thin films with (a) high adatom mobility, (b) low adatom mobility, taken from [13].

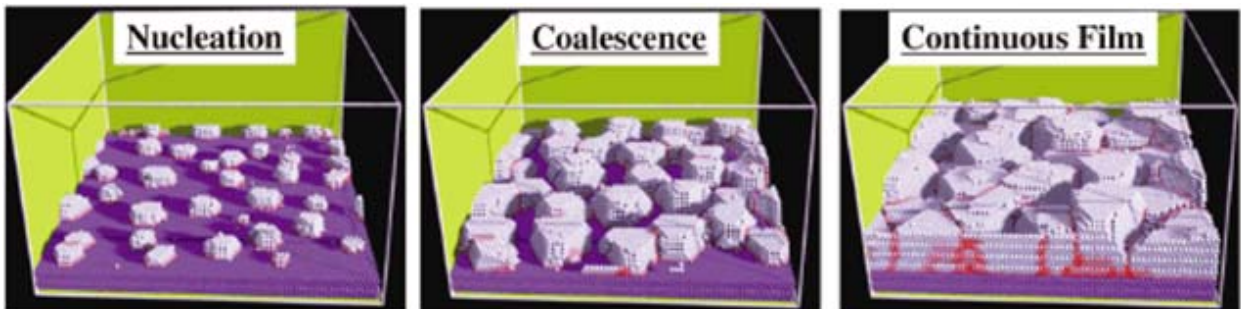


**Figure 1.3:** The microstructure evolution of thin films during Volmer-Weber growth, taken from [14].

### 1.2.1. Origins of pre-coalescence compressive stress

Two explanations are available for the origins of the first stage pre-coalescence compressive stress. Cammarata *et al.* [13] suggested that this stress is because of the surface having a “locked in” stress from the traction at the island-substrate interface. Since atoms of a solid in the vicinity of the surface have a bonding environment different than that of atoms within the interior, the surface atoms generally have an equilibrium inter-atomic distance different from the bulk value. When the island grows to one thickness,  $h_0$ , it has one corresponding lattice constant,  $a_0$ . However, if the film grows to another thickness,  $h_1$ , there will be another equilibrium lattice constant,  $a_1$ . However, because the island is rigidly bonded the substrate, its lattice parameter remains frozen at its previous point  $a_0$  value. This difference in lattice parameter will cause compressive stress formation [13,14].

Another explanation for the origin of the initial compressive stress is from Thompson *et al.* [15, 16]. In this model, it is proposed that the compressive stress is associated with the adatom-surface interactions and the stress is a function of the changes in the adatom population. In the beginning of thin film growth, the adatom concentration on the substrate rapidly increases. These adatoms cause the compressive stress. This mechanism is even generalized to the coalescence and post-coalescence growth regions, at which they argue that the adatom population changes affect the stress evolution for all stages in thin film growth [16].

### 1.2.2. Origins of intrinsic tensile stress upon island coalescence

Compared to compressive stress, the intrinsic tensile stress is better understood. For the tensile stress during island coalescence, it is generally explained by the “tradeoff” between surface energy and elastic energy. During thin film growth, the islands tend to form relatively low energy grain boundaries rather than discrete island surfaces, at the expense of the bending of

islands, which introduces extra strain energy [17]. Using this energy minimization analysis, the intrinsic stress associated with islands coalescence is estimated as [18]:

$$\sigma_{intrinsic} = \sqrt{\frac{M(2\gamma_s - \gamma_{GB})}{r}} \quad (1.1)$$

where  $\gamma_s$  and  $\gamma_{GB}$  are the surface and grain boundary energy for the thin films,  $r$  is the grain radius, and  $M$  is the biaxial modulus of the film. Note that equation (1) is an over-estimation of the stress because of the competing compressive stress.

In order to make a better estimation, Nix and Clemens [19] proposed a more complicated model by treating the grain boundary formation as a crack-closure process. At the point of grains boundary contact, the surface of adjacent grains is considered as a crack in an elastic medium. Under Griffith's energy minimization criterion, this "crack" will only zip up if the elastic bending energy is lower than the surface energy. This yields close agreement to the experimental tensile data, but with values tend to have a predicted higher tensile stress because of the complicated geometries of the thin films.

Frend and Chason have also proposed a model [20] which is based on the idea that the contact of elastic bodies has a cohesive attraction. By considering the geometries of the thin film grains, the estimation is in closer agreement to the experimental results as compared to the previous models. Arguably, the mechanism of tensile stress is well understood, *e.g.* tensile stress is formed by the impingement of grains to minimize surface energy area. The predicted stress values deviate from experimental values depending on the model chosen and these difference likely are a result of the over simplifying assumptions to model the thin film microstructure.

### 1.2.3. Origins of post-coalescence compressive stress

The origin of the post-coalescence compressive stress is the least understood. Though several mechanisms [10,15,16,21-24] have been proposed to explain the post-coalescence

compressive stress and stress relaxation during thin film growth interruption, none of them can explain all the phenomenon observed in experiments [24]. Currently, three main competing models are available for explaining the origins of the compressive stress during continuous thin film growth stage.

- (i) Locked-in capillarity stress model. Thompson *et al.* [15] proposed that the post-coalescence compressive stress is because of the locked adatom-surface interactions at the substrate and at the thin film surface. This was based on the observation that the magnitude of the pre-coalescence compressive stress-thickness product is similar to that of the post-coalescence region and both compressive stresses are reversibly relaxed during growth interruption. The stress changes during thin film growth and growth interruption are related to the adatom population. However, this mechanism fails to account for the tensile stress relaxation during thin film growth interruptions [15-16, 21].
- (ii) Recrystallization model. Considering thin film growth experiments with Fe, Koch *et al.* [21] observed that during film growth interruption, the value of the relaxation tensile component increases with thin film thickness and grain size. Thus, they proposed that recrystallization and grain growth played an important role in the latter stage compressive stress evolution and relaxation [21,25]. However, as pointed by C. V. Thompson *et al.* [24] and F. Spaepen *et al.* [26], recrystallization process is not reversible. Therefore, this mechanism fails to explain the reversible stress evolution during thin film growth interruption.
- (iii) Grain boundary insertion mechanism. This model proposes that extra atoms, driven by deposition flux, move in and out of grain boundaries during thin film growth and

growth interruption, as shown in Figure 1.4. According to Chason *et al* [10], the driving force for those extra atoms to the grain boundaries is from the increase in surface chemical potential because of the arrival and flow of deposited atoms on the surface. The chemical potential difference between the surface and grain boundaries is:

$$\Delta\mu = \mu_s - \mu_{gb} = \Delta\mu_0 + \delta\mu_s + \sigma\Omega \quad (1.2)$$

where  $\Delta\mu_0$  is the difference between the surface and grain boundary chemical potential in absence of growth (usually small and negligible),  $\delta\mu_s$  is the increase in surface chemical potential because of the flux of deposited atoms,  $\sigma$  is the stress along the grain boundary, and  $\Omega$  is the atomic volume.

This model is able to explain the reversible stress relaxation as well as the effect of deposition rates on the stress. However, there are still challenges for this model since whether the grain boundary plays an important role in stress evolution is still under discussion [23].

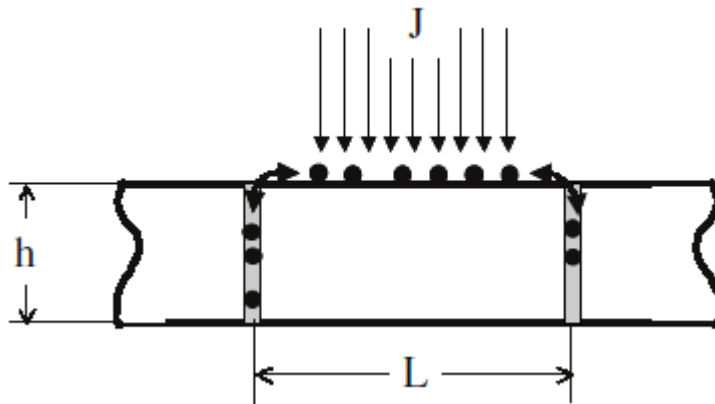


**Figure 1.4:** Schematic of model for flow atoms into the grain boundary during thin film growth.  $J$  is the impinge flux,  $L$  is the grain size, and  $h$  is the film thickness, taken from [10].

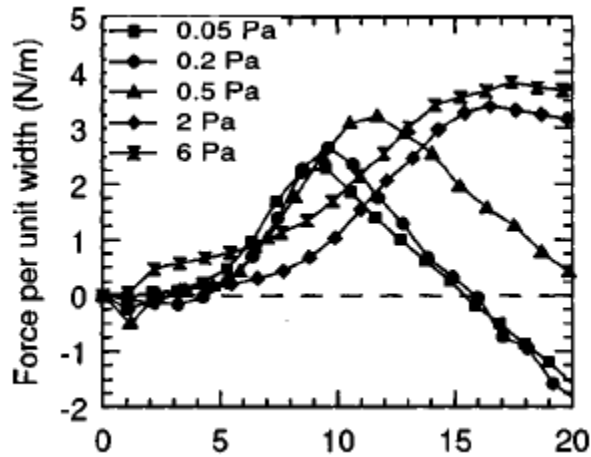


**Figure 1.5:** The evolution of film force of Cu thin films deposited at 0.1 nm/s with various deposition pressures, taken from [8].

### 1.3. Kinetic parameters

The microstructure of a thin film is dependent on the kinetic parameters at which it grows; therefore, the intrinsic stress is very sensitive to these experimental parameters. Deposition pressure, substrate temperature, deposition rate, thin film composition, and even background gases, such as oxygen content, can affect the intrinsic stress.

#### 1.3.1. The influence of deposition pressure

The kinetic energy of the impinged ions/atoms is associated with the deposition pressure. It will decrease with increasing deposition pressure. It should be noted that the deposition rates can also be affected by the deposition pressure. However, the discussion of deposition pressure on the stress evolution in the following is based upon constant deposition rate.

Since the kinetic energy is decreasing with the increase deposition pressure, *e.g.* the vapor atoms experience a shorter mean free path or, alternatively, more collisions with the deposition atmospheric pressure, the adatom mobility upon nucleation decreases. Therefore, the compressive intrinsic stress in the continuous growth stage becomes smaller and can even change to tensile with increasing deposition pressure. Figure 1.5 is such an example. It can be seen that at lower pressures, an intrinsic compressive stress develops at the post-coalescence region; however, at higher deposition pressures, only tensile stress can be seen after the thin film becomes coalescence. This transition from compressive stress to tensile stress is argued that the film undergoes a transition from a dense microstructure to more open microstructure [8]. Similar results have been reported to other systems as well [12].

#### 1.3.2. The influence of substrate temperature

The influence of substrate temperature on intrinsic stress is similar to that of deposition pressure. As the substrate temperature increases, the diffusion length of the impinged atoms

increases, which increases the adatom mobility. This increase in mobility increases the compressive stress after island impingement. Similarly, a thin film that experiences tensile stress at room temperature can change to compressive stress if grown at elevated temperature [21, 27-29].

In addition to the increase in adatom mobility, thin films grown at elevated temperatures may undergo phase transformations or form different microstructures. These changes will also show a stress behavior different than that of a film deposited at room temperature. Unfortunately, different microstructure evolutions will lead to different stress changes, which can only be studied case-by-case. For example,  $Ti_{50}Cu_{50}$  thin films grown at different substrate temperatures form amorphous and polycrystalline thin films, respectively, show different *in situ* stress behaviors [30].

### 1.3.3. The influence of deposition rates

Deposition rates may also have an effect on the evolution of intrinsic stress. Spaepen *et al.* [31] have deposited elemental Cu and Ag on Si substrates at different rates. It was observed that the deposition rates have no effect on the tensile stress evolution of both thin films. However, the coalescence thickness (maximum tensile stress) of the Ag thin films increased with deposition rates. The post-coalescence compressive stress of both thin films decreased with increasing deposition rates, but the magnitude in the Ag thin films was not as pronounced as that of Cu films. The stress changes with deposition rates of Cu and Ag thin films, which shows similar compressive-tensile-compressive stress evolution during growth, indicates that the stress evolution with deposition rates is complicated.

Moreover, not every model proposed predicts the same stress changes with deposition rates. For example, the locked-in capillarity stress model infers that the post-coalescence

compressive stress is not affected by deposition rates, which is contrary to the experimental results above. The grain boundary insertion mechanism does indicate that the post-coalescence compressive decreases with increasing deposition rates. However, whether this model itself is valid or not is still under discussion [31].

#### 1.3.4. Other factors

The influence of vacuum background gases and thin film composition on intrinsic stress evolution is complicated. The incorporation of trace gas atoms in the vacuum can cause the creation of defects reactions, such as oxidation, with the metal thin film during growth changing the typical stress behavior [32]. This is probably one reason that the intrinsic stress observation is very difficult to replicate since background gases are often not reported or measured from deposition-to-deposition.

Different metal atoms have different atom mobility and bonding energies. If various elements are deposited together to form alloy thin films, different phenomenon may occur such as competing adatom mobility, segregation of some elements to grain boundaries or free surfaces, ordering to form superlattices or multiphase formations because of thermodynamic phase separation. All these contribute to different intrinsic stress evolutions. While most of experimental research about intrinsic stress has been focused on single metallic elements, there is less information about metallic alloy systems [7-12,30] and is the focus of this thesis.

#### 1.4. Fe-Pt and Fe-Cu thin films

The first portion of this thesis addresses the composition dependent intrinsic stress state in a Fe-Pt and Fe-Cu alloy system. The Fe-Pt is a miscible and ordering system where as Fe-Cu is an immiscible system. The second portion of this thesis addresses the stress evolution during deposition at various *in situ* elevated substrate temperatures. When near equi-atomic FePt thin

films are grown at elevated temperatures, the film will order into the  $L1_0$  intermetallic phase. The phase transformation from A1, disordered face centered cubic structure, to  $L1_0$ , leads to a stress change. The relationship between intrinsic stress and the ordering phase is studied. The third portion of this thesis discusses the stress evolution of thin films during phase separation in a near equiatomic FeCu alloy at different *in situ* deposition substrate temperatures. The stress evolution is studied and explained by the microstructure evolution. Finally, the results of each system are summarized in the last chapter as well as future direction of the research.

## CHAPTER 2

### EXPERIMENT DETAILS

In this chapter, the materials and instruments used in the experiments are described in details. The experimental setup of the instruments and the measurement principles are described. This chapter is divided into three parts: thin film growth, stress measurement and structural characterization.

#### 2.1. Thin film growth

The thin films were grown in an AJA ATC-1500 stainless-steel chamber with a base pressure  $< 1 \times 10^{-7}$  Torr, as seen in Figure 2.1. The substrate used was Si [100] that had a thickness of about 300  $\mu\text{m}$ . The metal thin films were DC magnetron sputter-deposited from elemental targets with  $> 99.5\%$  purity. The alloy films were done by confocal co-sputter deposited from each respective elemental target. During deposition, ultrahigh purity Ar was flowed at 10 sccm to 2 mTorr as the working gas to generate the plasma.

Prior to the deposition of the metal thin films grown at elevated temperatures, a 10 nm  $\text{Si}_3\text{N}_4$  barrier layer was RF sputter deposited and acted as a diffusion barrier layer to prevent any deleterious silicide reactions between the substrate and metallic film to occur. For the thin films studied in Chapter 3 (the studies of compositional dependent stress states at ambient temperature), the metallic thin films were deposited directly on the Si substrates. For films grown at temperature, the temperature of substrate, prior to film deposition, was measured using the non-contact K-space Associates BandiT system, which monitors the Si band gap absorption edge to determine the temperature of the wafer.

## 2.2. Thin film Stress Measurement

The *in situ* growth stress and post growth stress relaxation were measured by k-space Associates' Multi-beam Optical Sensor (MOS) system mounted inside the sputtering chamber. The MOS system is the substrate bending measurement technique, whose principle is the well known Stoney's equation [33]:

$$\sigma = -\frac{1}{12} \frac{E_s}{1-\nu_s} \frac{t_s^2}{L t_f} \left( \frac{1}{R_1} - \frac{1}{R_0} \right) \quad (2.1)$$

where  $E_s/(1-\nu_s)$  is the biaxial modulus of the substrate,  $t_s$  and  $t_f$  are the thickness of the substrate and thin film respectively,  $L$  is the substrate-detector optical length,  $R_0$  and  $R_1$  are the radius of curvature of the measured substrate before and during/after film deposition.

To measure the curvature change, the MOS system uses a laser that produces a linear array of parallel beams formed from an etalon. The laser rays reflect off the sample surface and are captured by a CCD camera, seen in figure 2.2. As the curvature changes, the laser rays spatial positions move and the curvature, hence stress, is measured. The laser spots are captured using a high-resolution CCD detector that enables the MOS system to easily detect the changes in laser spot position with micro-meter precision. This MOS technique is able to perform real-time stress measurement during and after thin film growth [34].

The input parameters for equation 2.1 above are the following: The distance between the detector and the substrate,  $L$ , is 38 cm, the biaxial modulus of the substrate was 180 GPa [35], and the thickness of the Si [100] substrate was  $\sim 300 \mu\text{m}$ .

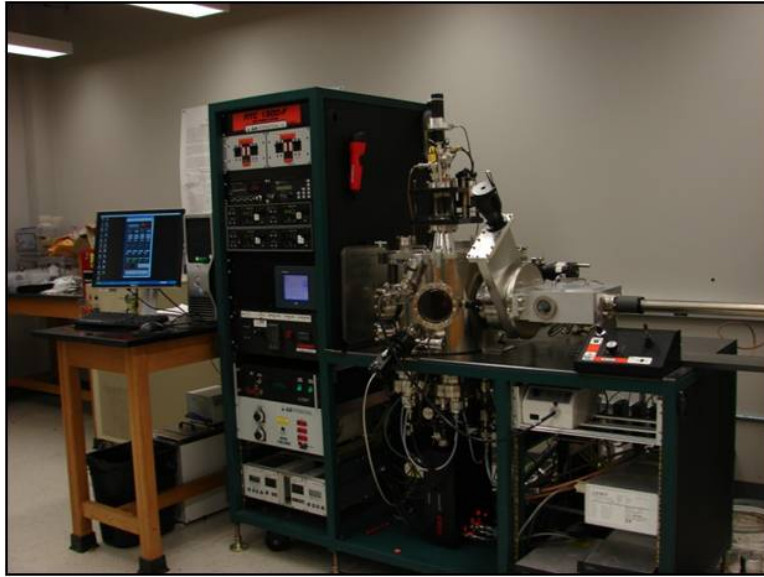


**Figure 2.1:** The AJA ATC-1500 sputtering system used in the experiments.

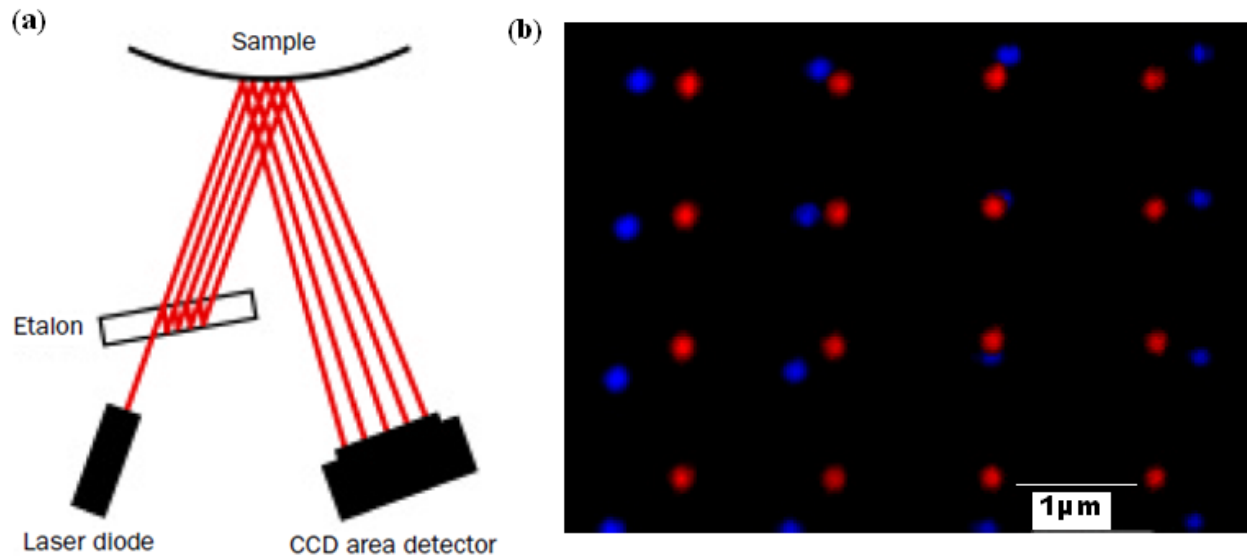


**Figure 2.2:** (a) Schematic description of the setup of the MOS: the etalon split the original laser beam into an array of parallel laser beams, which reflect off the sample surface and are imaged by a CCD area detector; (b) Superposition of laser spots imaged by CCD detector from a silicon surface before (red) and after (blue) the wafer has been stressed, taken from [34].

### 2.3. Structural Characterization

The phase and estimated grain size of the thin films was characterized by X-ray Diffraction (XRD) and the microstructure was characterized by transmission electron microscopy (TEM), atom probe tomography (APT) and atom force microscopy (AFM).

#### 2.3.1. Quantification of thickness and composition

The thickness of these thin films was estimated by the deposition rate and verified by small angle X-ray reflectivity [36] using an X'Pert Philips X-ray diffractometer operated with a Cu  $K_{\alpha}$  source at 45 keV and 40 mA. The composition of the alloy thin films was also controlled by the deposition rate from each single elemental target. The average composition of the thin films was verified using scanning electron microscopy - energy dispersion spectrometry (SEM - EDS) using a Philips XL30 operated at 20 keV.

#### 2.3.2. Microstructure analysis

The phases of these thin films were determined by XRD using Bruker Discovery D8 General Area Diffraction Detector System (GADDS) that utilized either Co or Cu  $K_{\alpha}$  radiation as the source. In addition selected area electron diffraction (SAED) patterns were taken using a Tecnai F20 (S)TEM. The in-plane grain size of the thin films grown at room temperature was calculated from the XRD data using the Williamson and Hall method [37]. The value of these grain sizes were verified by TEM bright and dark field images.

The TEM foils were prepared in two orientations: plan-view and cross-section. The procedure to make TEM plan-view samples is as follows: A 3 mm disc was cut out from the substrate where upon it was ground to about 100  $\mu\text{m}$  thick from the Si side using 600 grit SiC paper on a polishing wheel. The disc was then dimpled grind to about 15  $\mu\text{m}$  thick in the center

for the Si back side. Finally, the sample was polished until perforation to create electron transparency using Ar ions in a Gatan Precise Ion Polishing System (PIPS) at energies of 2-4 keV at an incident angle from 5-10 degrees.

The TEM cross-section samples were made using the FEI Quanta 3D dual-beam FIB - SEM. Prior to the preparation process, the thin films were coated with a Cr or Ni 500 nm sacrificial layer to protect the thin films from the Ga ion focused beam. In the FIB, a wedge that was approximately 20  $\mu\text{m}$  long and 2  $\mu\text{m}$  wide was cut out of the sample. Then the sample was mounted to a Cu grid and thinned to about 200 nm with the ion beam at 30 keV and current setting at 0.5 nA to 0.1 nA. The sample was put into the Gatan PIPS for a “cleaned-up” (remove Ga damage surface) with beam energies of approximately 2 keV at an angle of 7 degrees.

The atom probe tips were analyzed in an Imago Scientific Instruments Local Electrode Atom Probe (LEAP®) 3000XSi in a laser pulsing mode. The field evaporation events were run at a base temperature of 50 K with laser pulse energy of 0.3-0.5 nJ at a pulse rate of 250 kHz. Lower base temperatures and lower pulse energies resulted in a propensity of tip fracture failures during field evaporation. The tips were made by annular focus ion beam milling using a FEI Quanta 3D dual beam FIB – SEM. Similarly to the TEM cross-sections, a Cr or Ni 500 nm protection layer was deposited onto the surface of the film and a 30  $\mu\text{m}$  long, 3  $\mu\text{m}$  wedge was lifted-out from the sample. The cut out wedge was extracted from the film/substrate using *in situ* micromanipulation and then mounted as individual pillars onto flat top Si posts. The tips were shaped by annular milling at 30 keV and currents of 0.3-1 nA. A final 5 keV “clean up” step was used to reduce the Ga damage in the sample. The details of the procedure can be found in references [38, 39].

The surface roughness of the film was measured by AFM in the tapping mode using a Park Scientific Instruments AFM. The surface roughness is represented by root mean square (rms) value determined over  $1 \mu\text{m}^2$  area obtained at 0.5 Hz.

## CHAPTER 3

### COMPOSITIONAL DEPENDENT STRESS STATES

In this chapter, the as-deposited *in situ* stress measurements of two binary alloy systems, Fe-Pt, a miscible system, and Fe-Cu, an immiscible system, are studied. As described above, most of experimental research about *in situ* stress has been focused on single metallic element. There is less information about metallic alloy systems. Alloys can result in co-operative adatom mobility for different species which will result in different growth stresses. The coordination of alloy content could be used to tune the growth stresses in thin films. This similar stress behavior was observed in both the Fe-Pt alloy system and Fe-Cu alloy system.

#### 3.1. Results

##### 3.1.1. The Fe-Pt System

The *in situ* stress evolution of the 40 nm thick Fe, Pt, Fe<sub>54</sub>Pt<sub>46</sub> and Fe<sub>65</sub>Pt<sub>35</sub> thin films is displayed in figure 3.1(a). From this figure, the Fe thin film experiences a compressive-to-tensile stress transition and the Pt thin film exhibits a compressive-to-tensile-to-compressive stress transition, which is consistent with similar reports in the literatures [7,11]. The co-sputtering of Fe and Pt formed a solid solution alloy as will be later shown in the XRD and electron diffraction figures. These alloys had a stress state that was bounded by the two extremes of the elemental films, as seen in figure 3.1(b). It is found that the Fe<sub>65</sub>Pt<sub>35</sub> thin film showed a residual stress near zero at 40 nm thickness.

Since deposition rates can affect the mobility of adatoms therefore the stress state, the ‘zero-stress’ Fe<sub>65</sub>Pt<sub>35</sub> thin film was deposited at two different rates that span an ~ 2X difference from 0.08 nm/s to 0.15 nm/s. Similar to the single element films [10,31], the growth stress changed with the deposition rates. For the rates explored, this change was very minor, as seen in figure 3.2. The XRD results of the as-deposited thin films for the four different compositions are plotted in figure 3.3. Each film is highly textured with the closest packed planes being parallel to the growth direction. The elemental Fe film was indexed as bcc where as the elemental Pt was fcc and the Fe<sub>x</sub>Pt<sub>100-x</sub> compositions grown were indexed as the random solid solution fcc phase denoted as A1. This A1 phase is consistent with the literature [40] and is the quenched-in high temperature phase for this system. The in-plane grain size of these thin films were very similar with values that ranged from ~12 nm to ~14 nm, as tabulated in table 3.1. TEM bright field images, shown in figure 3.4(a), confirmed the XRD grain size analysis. The TEM selected area electron diffraction patterns, figure 3.4(b), confirmed the XRD result that the Fe<sub>65</sub>Pt<sub>35</sub> film was A1 as evident by the ratio of the ring spacing being consistent with the fcc symmetry.

The AFM results, shown in figure 3.5, indicated that the film near zero stress was smoother than either the compressive or tensile films. The root mean square (rms) roughness of the Fe, Pt, Fe<sub>65</sub> Pt<sub>35</sub> and Fe<sub>54</sub>Pt<sub>46</sub> films were 0.18 nm, 0.37 nm, 0.09 nm and 0.11 nm respectively.

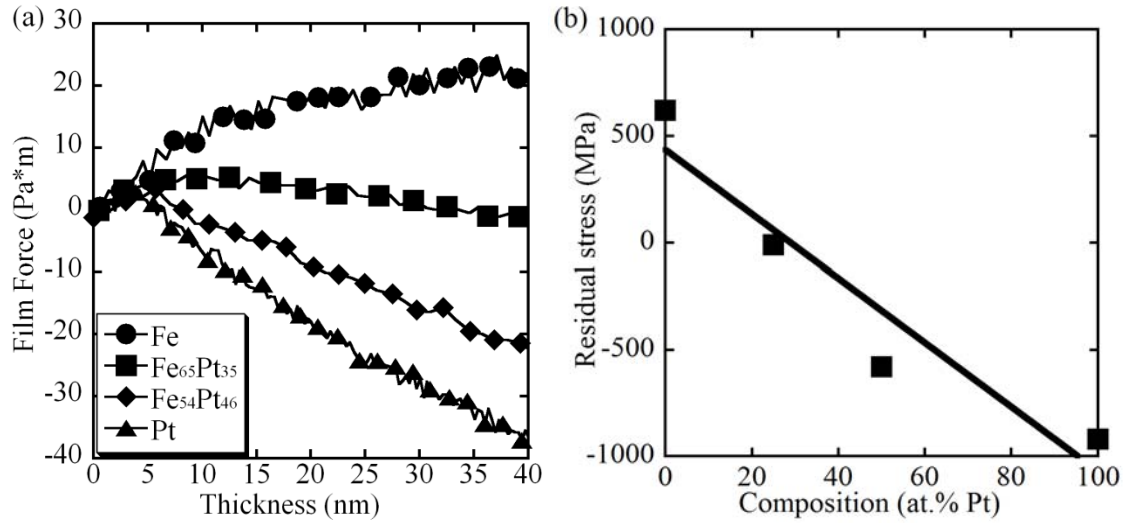


**Figure 3.1:** (a) Evolution of growth stresses of the Fe-Pt system thin films. (b) Residual intrinsic stresses measured at the end of the depositions of a 40 nm film. The deposition rates for the Fe, Fe<sub>65</sub>Pt<sub>35</sub>, Fe<sub>54</sub>Pt<sub>46</sub> and Pt thin films are 0.1 nm/s, 0.15 nm/s, 0.18 nm/s and 0.05 nm/s respectively. Note that the residual stress varies as a function of composition.

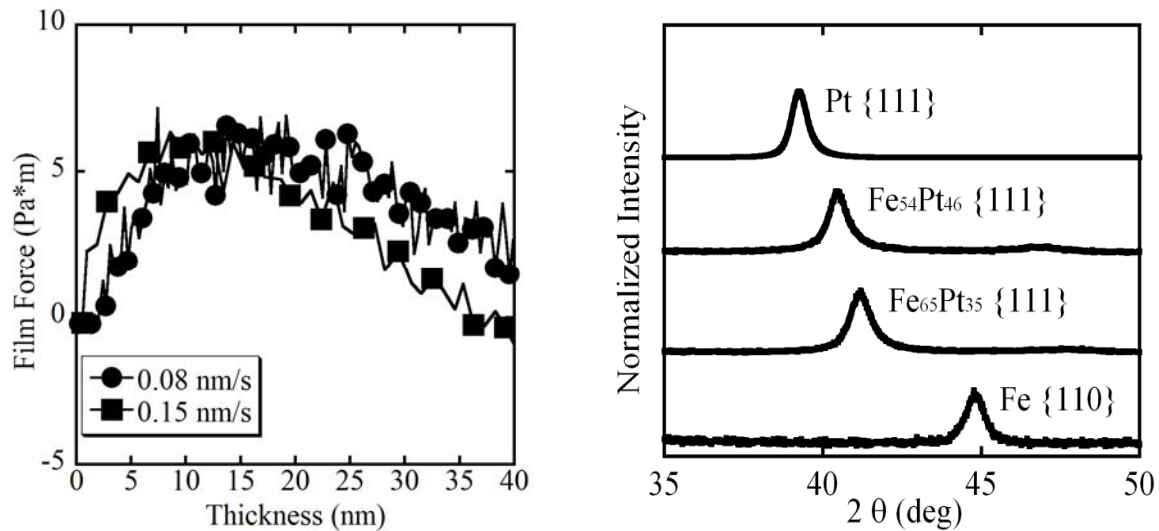


**Figure 3.2:** Evolution of growth stresses of Fe<sub>65</sub>Pt<sub>35</sub> thin films grown at different deposition rates.

**Figure 3.3:** XRD profiles of as-deposited Fe, Fe<sub>65</sub>Pt<sub>35</sub>, Fe<sub>54</sub>Pt<sub>46</sub> and Pt thin films using Cu K $\alpha$  X-rays.

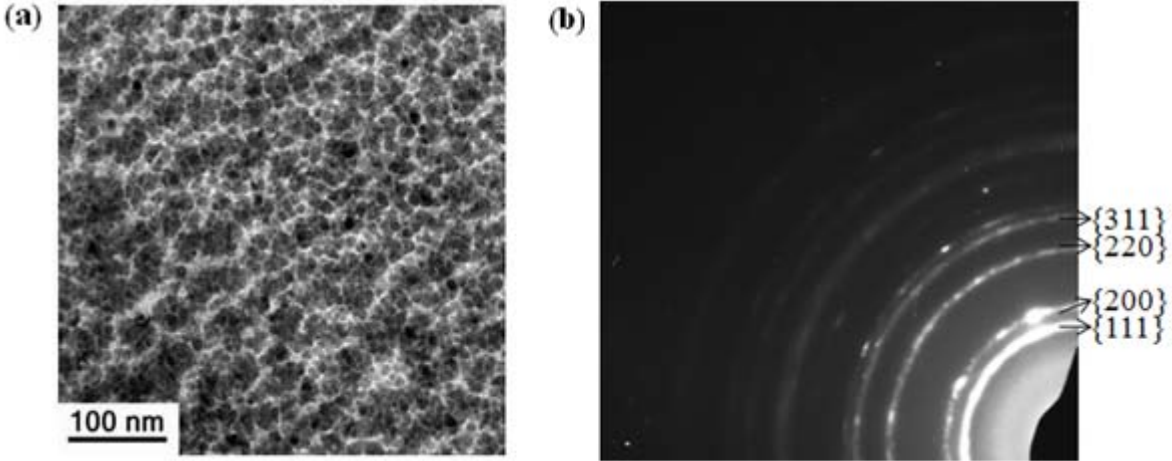


**Figure 3.4:** (a) TEM bright field image and (b) selected area electron diffraction pattern of the  $\text{Fe}_{65}\text{Pt}_{35}$  as-deposited thin film. The bright field image shows an average grain size about 10 nm and the diffraction pattern shows the fcc symmetry.

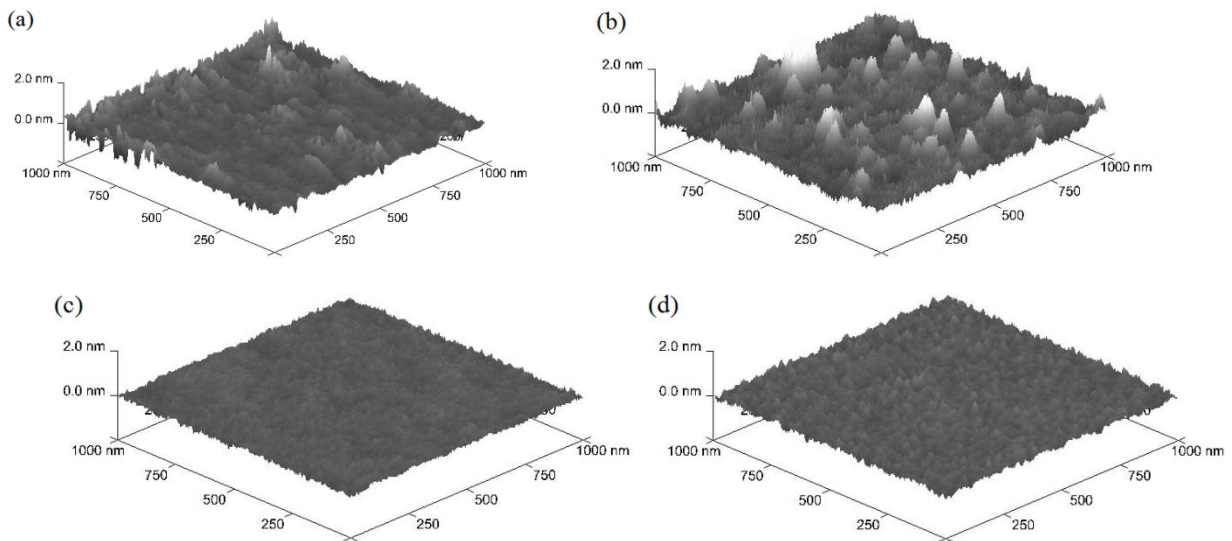


**Figure 3.5:** AFM micrographs of Fe-Pt films imaged using the tapping mode. (a) Fe (b) Pt (c)  $\text{Fe}_{65}\text{Pt}_{35}$  (d)  $\text{Fe}_{54}\text{Pt}_{46}$ , the roughness of these thin films are 0.18nm, 0.37nm, 0.09nm, and 0.11nm respectively.

The LEAP results are shown in figure 3.6. The reconstructed Pt atom map clearly shows the grain boundaries in the Fe<sub>54</sub> Pt<sub>46</sub> thin films. Previous TEM Fresnel contrast imaging of a thin film atom probe tip of a similar composition has confirmed that these density variations are consistent with the shape, size and density increases in the grain boundaries that are reconstructed from the atom probe [39]. The grain size in these atom maps, figure 3.6(a), is consistent with those measured using XRD analysis given in table 3.1. The density variations in the atom maps are trajectory aberrations that can result from density variations, compositional variations and/or surface variations [41-43]. The 1D compositional profile of a grain boundary in Fe<sub>54</sub> Pt<sub>46</sub>, figure 3.6(b), shows an enrichment of Pt, which is consistent with literature [39]. However, for the Fe<sub>65</sub> Pt<sub>35</sub> thin film, it is difficult to distinguish the grain boundaries from the atom map reconstructions. The 1D compositional profiles for Fe<sub>65</sub> Pt<sub>35</sub>, across the entire atom map does not show any significant variations in composition. Based on the grain size of this film and the field of view of the atom map, the profile would intersect several grain boundaries. For the elemental Pt thin film, very distinct grain boundaries can be seen in the reconstructed atom map of figure 3.6(f). The elemental Fe thin film does not show distinct grain boundaries in the atom map of figure 3.6(h).

**Table 3.1:** The average residual stress measured at the end of the deposition and the average grain size calculated using Williamson and Hall method [37] for the Fe-Pt thin films with various compositions.

<b>Composition (at.%)</b>	<b>Fe</b>	<b>Fe<sub>65</sub>Pt<sub>35</sub></b>	<b>Fe<sub>54</sub>Pt<sub>46</sub></b>	<b>Pt</b>
<b>Residual stress (MPa)</b>	612	-10	-580	-980
<b>Average grain size (nm)</b>	14	9	14	9.5

**Table 3.2:** The average residual stress measured at the end of the deposition and the average grain size calculated using Williamson and Hall method [37] for the Fe-Cu thin films with various compositions.

<b>Composition (at.%)</b>	<b>Fe</b>	<b>Fe<sub>65</sub>Cu<sub>35</sub></b>	<b>Fe<sub>50</sub>Cu<sub>50</sub></b>	<b>Cu</b>
<b>Residual stress (MPa)</b>	612	112	-24	-320
<b>Average grain size (nm)</b>	14	13.8	11.5	11.9

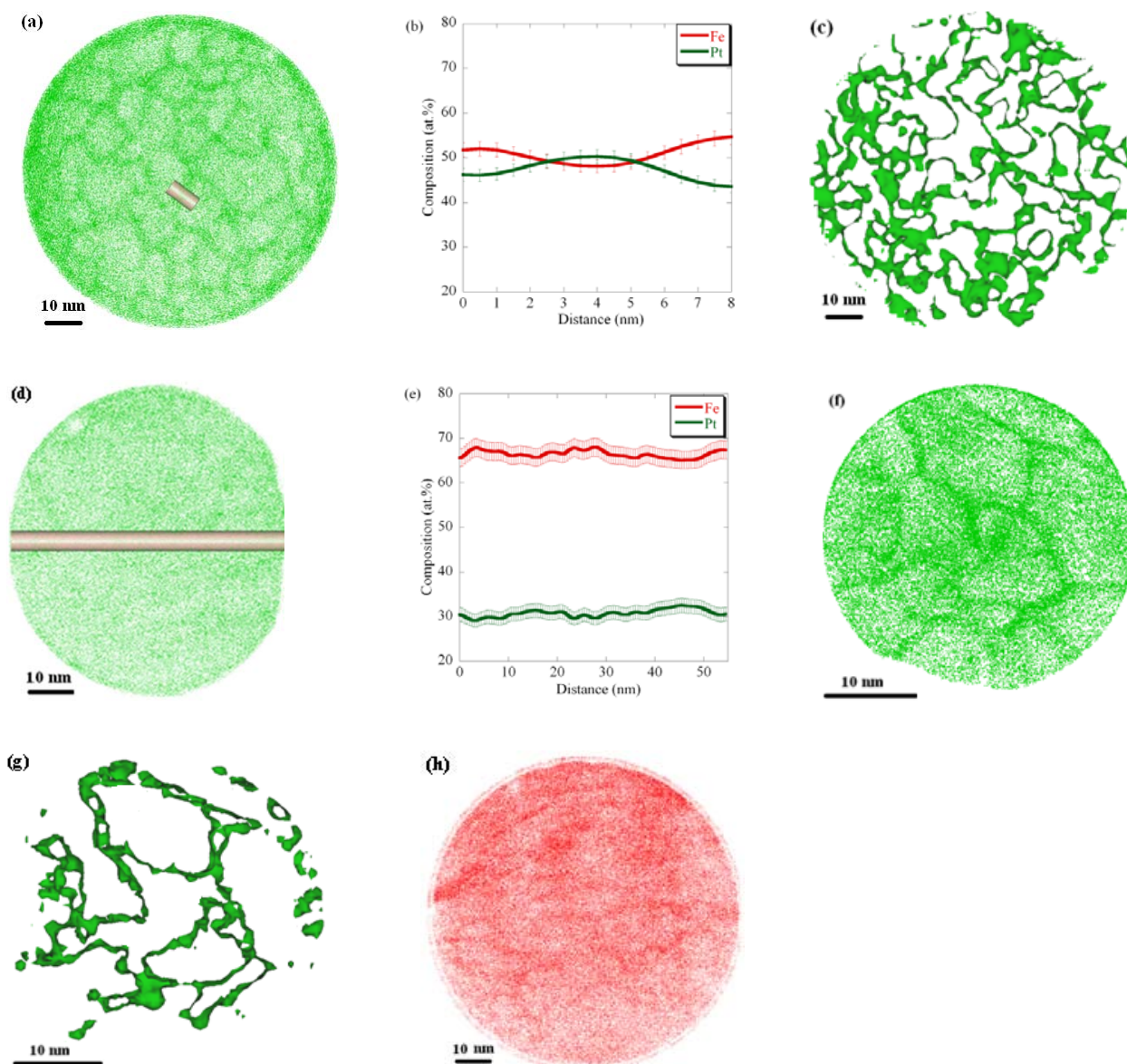


**Figure 3.6:** (a) Pt atom map in the  $\text{Fe}_{54}\text{Pt}_{46}$  film (b) 1D compositional profile from (a) (c) Iso-concentration surface created at 47.2 at.% Pt, which is higher than the average Pt content. The iso-surface maps closely the density variations (grain boundaries) in (a). (d) Pt atom map in the  $\text{Fe}_{65}\text{Pt}_{35}$  film (e) 1D compositional profile from (d) (f) Pt atom map in the pure Pt film (g) Iso-density surface created at higher than the average Pt density. The iso-surface maps closely the density variations (grain boundaries) in (f). (h) Fe atom map for the Fe film.

### 3.1.2. The Fe-Cu systems

Unlike the Fe-Pt thin films, which can form a miscible solid solution, the Fe-Cu alloy is thermodynamically immiscible. Since sputtering is a non-equilibrium process, meta-stable mixing can result, which was confirmed by the XRD scans in figure 3.7 and the electron diffraction patterns in figures 3.8 and 3.9. Similar to the Fe-Pt system, the Fe-Cu alloys exhibit a composition dependent stress state between the two extremes of the elemental Fe and Cu stress values. In this case, the Cu film, like the Pt film, was the compressive elemental film. A near zero-stress state at 40 nm was found to occur at Fe<sub>50</sub>Cu<sub>50</sub>. The composition dependent stress states have been plotted in figure 3.10. The variation of this ‘zero stress state’ over 3X deposition rates that span 0.09 nm/s - 0.27 nm/s was minor and is plotted figure 3.11. This result is similar to the previous Fe-Pt deposition rate dependence on the ‘zero stress state,’ that is that the stress state is relatively insensitive to changes in the deposition rates investigated.

The average grain sizes of the Fe-Cu thin films ranged from ~9 nm to ~14 nm and are tabulated in table 3.2. The TEM micrographs in figures 3.6 and 3.7 confirmed the XRD grain (crystallite) size estimation. The selected area electron diffraction patterns verified the bcc phase for the Fe<sub>65</sub>Cu<sub>35</sub> film and the fcc phase for the Fe<sub>50</sub>Cu<sub>50</sub> film as evident by the ratio of the ring spacing being consistent with those symmetries

An atom map of the Fe<sub>50</sub>Cu<sub>50</sub> film, the zero stress condition, is shown in figure 3.12(a) with a 1D compositional profile that spans the entire atom map, figure 3.12(b). Similar to the zero stress film for Fe<sub>65</sub>Pt<sub>35</sub>, the LEAP data does not reveal any significant compositional fluctuations. Based on the field of view and grain size, the compositional profile would intersect several boundaries.

Similar to the Fe-Pt results, AFM results indicated that the film near zero stress was smoother than either the compressive or tensile films, as seen in figure 3.13. The rms roughness of the Fe, Cu, and Fe<sub>50</sub>Cu<sub>50</sub> films were 0.18 nm, 0.21 nm, and 0.15 nm respectively.

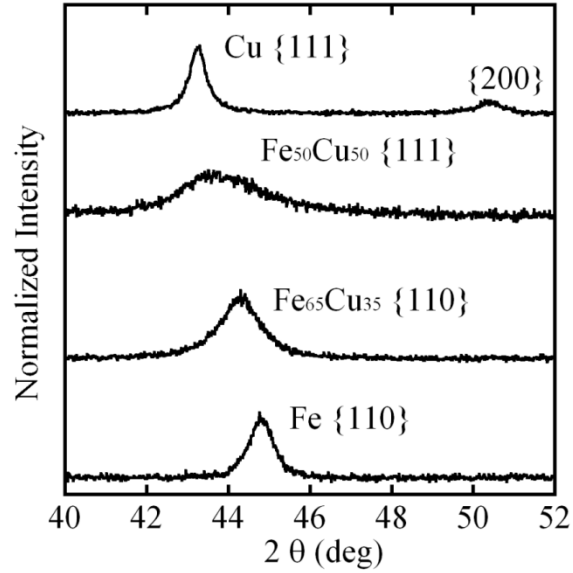


**Figure 3.7:** XRD profiles of the as-deposited Fe,  $\text{Fe}_{65}\text{Cu}_{35}$ ,  $\text{Fe}_{50}\text{Cu}_{50}$  and Cu thin films using Cu  $K\alpha$  X-rays.

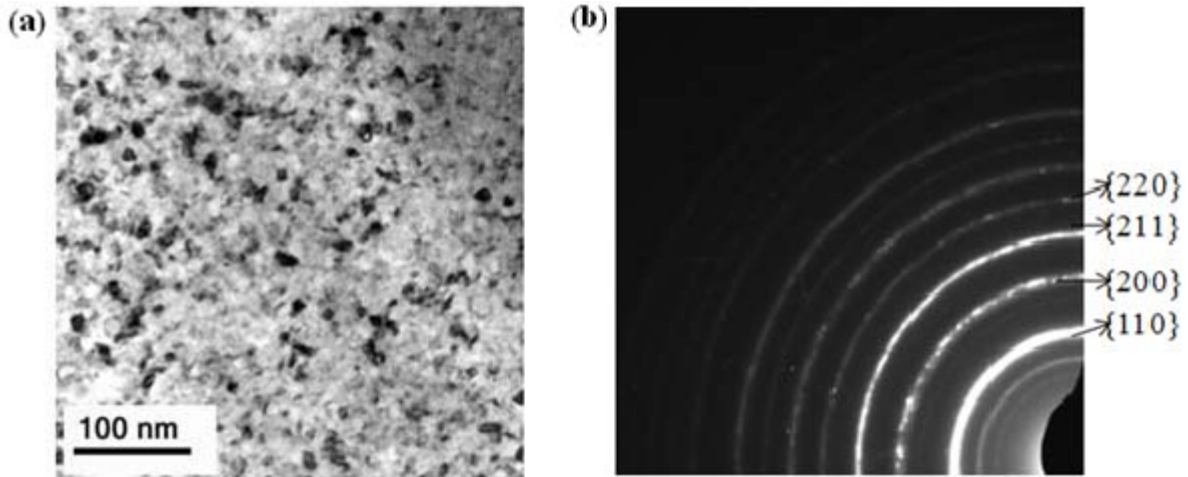


**Figure 3.8:** (a) TEM bright field image and (b) Selected area electron diffraction pattern of the  $\text{Fe}_{65}\text{Cu}_{35}$  thin film. The bright field image shows an average grain size about 10 nm and the diffraction pattern shows the bcc symmetry. The weak, un-indexed peaks between the  $\text{Fe}_{65}\text{Cu}_{35}$  peaks are  $\text{Fe}_2\text{O}_3$  diffraction peaks, unintentionally introduced during the TEM foil preparation process.

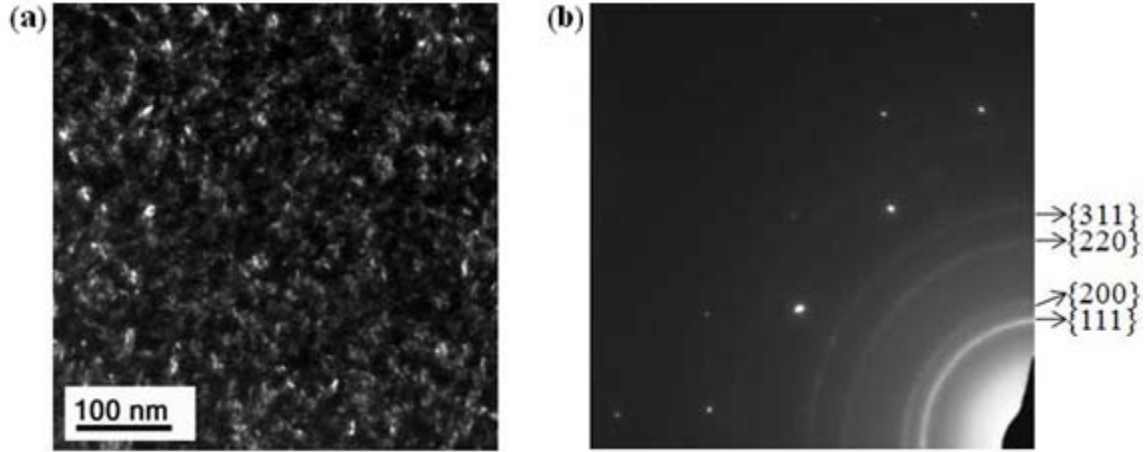


**Figure 3.9:** (a) TEM dark field image and (b) Selected area electron diffraction pattern of the  $\text{Fe}_{50}\text{Cu}_{50}$  thin film. The dark field image shows an average grain size of about 10 nm and the diffraction pattern shows the fcc symmetry. The intense diffraction spots are from the single crystal Si substrate.

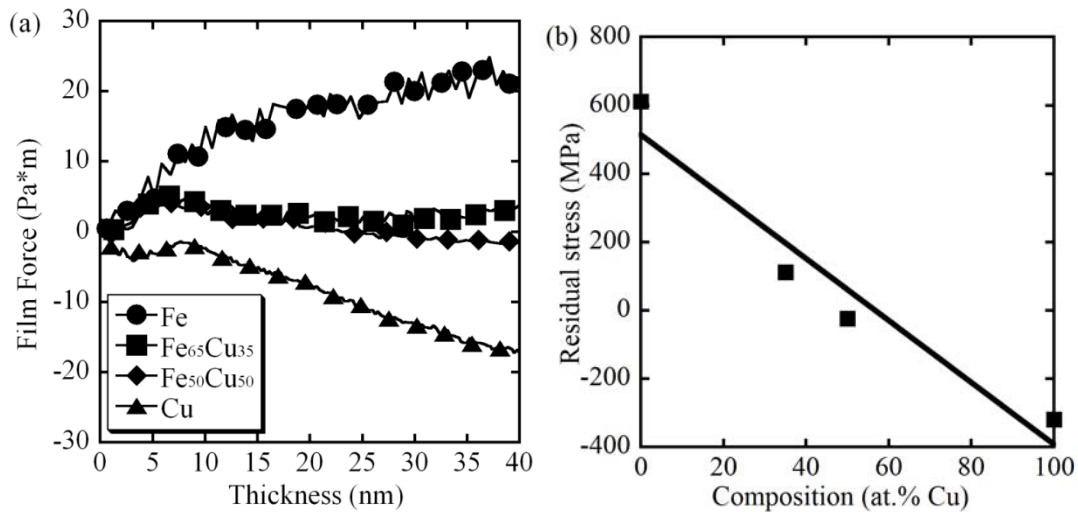


**Figure 3.10:** (a) Evolution of growth stresses of the Fe-Cu system thin films and its dependence on composition. (b) Residual intrinsic stresses measured at the end of the depositions of a 40 nm film. The deposition rate for the Fe,  $\text{Fe}_{65}\text{Cu}_{35}$ ,  $\text{Fe}_{50}\text{Cu}_{50}$  and Cu thin films are 0.1 nm/s, 0.15 nm/s, 0.18 nm/s and 0.08 nm/s respectively.

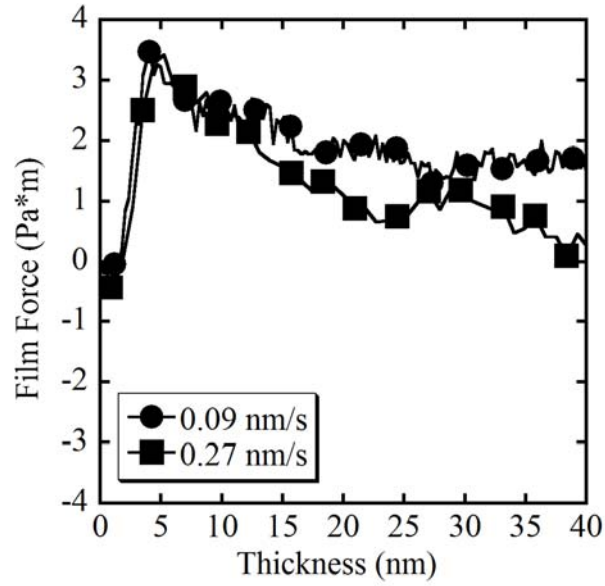


**Figure 3.11:** Evolution of growth stresses of the  $\text{Fe}_{50}\text{Cu}_{50}$  thin films at different deposition rates.

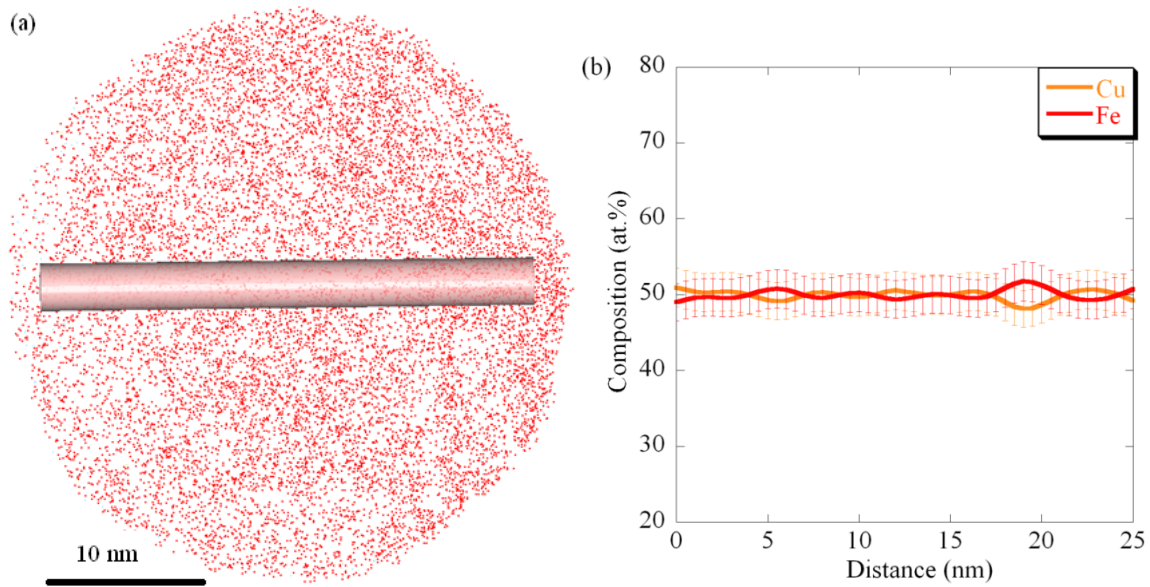


**Figure 3.12:** (a) Fe atom map of the  $\text{Fe}_{50}\text{Cu}_{50}$  film (b) 1D compositional profile from (a).

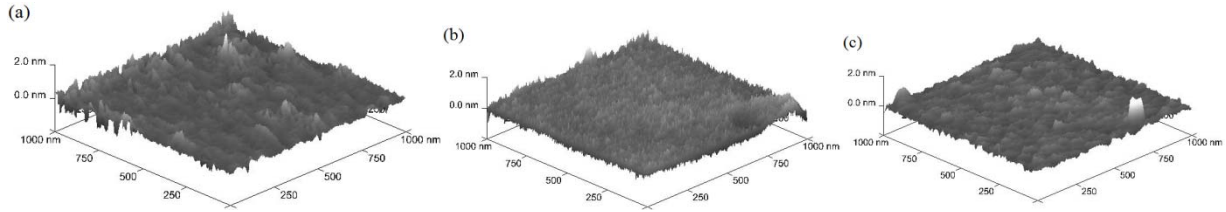


**Figure 3.13:** AFM micrographs of Fe-Cu films imaged using the tapping mode (a) Fe (b) Cu (c)  $\text{Fe}_{50}\text{Cu}_{50}$ . The roughnesses of these thin films are 0.18nm, 0.21nm and 0.15 nm respectively.

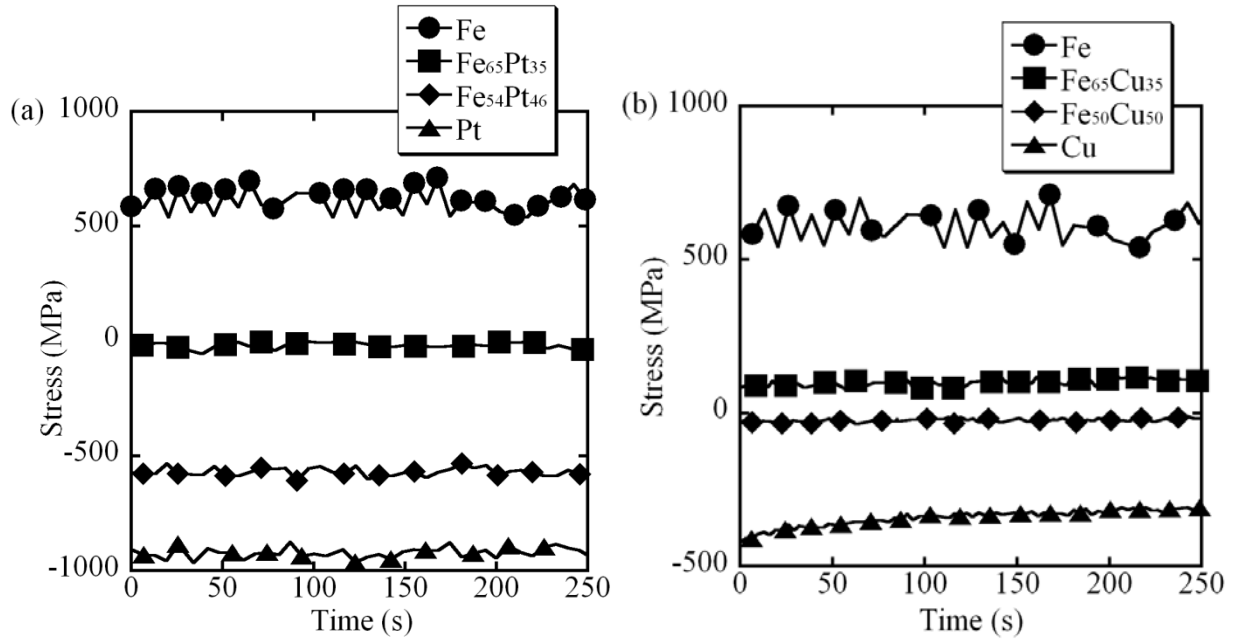


**Figure 3.14:** The evolution of the average intrinsic stress after the deposition of the thin films with a final thickness of 40 nm for: (a) the Fe-Pt system and (b) Fe-Cu system.

### 3.2. Discussion

The *in situ* stress measurements for the Fe-Pt and Fe-Cu alloy thin films are strongly dependent on their compositions. These alloy stress states are bounded by the extremes of the elemental films' stress state. There has been considerable discussion in the literature on the origins of these stress states. Chason *et al.* [10] have proposed that the compressive stress during post-coalescence is caused by the adatoms reversibly moving in and out of the grain boundaries. The driving force for those extra atoms to the grain boundaries is from the increase in surface chemical potential because of the arrival and flow of deposited atoms on the surface [10]. The experimental results of this chapter have been interpreted in terms of Chason *et al.*'s model [10].

The chemical potential difference between the surface and grain boundaries for a binary alloy system can be rewritten as [10]:

$$\Delta\mu' = \mu_s - \mu_{gb} = \Delta\mu_0 + \delta\mu_s + \sigma\Omega - \mu_c \quad (3.1)$$

where  $\Delta\mu_0$  is the difference between the surface and grain boundary chemical potential in absence of growth (usually small and negligible),  $\delta\mu_s$  is the increase in surface chemical potential because of the flux of deposited atoms,  $\sigma$  is the stress along the grain boundary,  $\Omega$  is the atomic volume, and  $\mu_c$  is chemical potential rise in the grain boundary because of the aggregation of extra, high adatom mobility atoms. We have added the latter term,  $\mu_c$ , to describe the chemical potential driving force of preferential segregation of one species to another to the boundaries.

For a binary alloy, differences in intrinsic mobility between each species can induce preferential segregation of the higher mobile species to the grain boundaries. This grain boundary segregation yields an additional chemical potential. For highly mobile films, like Pt, the addition of Fe changes the grain boundary chemical potential and can reduce the force that is driving atoms towards the grain boundaries. Alternatively, the low mobility films, like Fe, can

have their grain boundary chemical potential facilitate the mobility of atoms to the boundary by the addition of Pt. The atom probe tomography grain boundary analysis of Fe<sub>54</sub>Pt<sub>46</sub> thin films indicated a preferential segregation of Pt above the bulk Pt film composition at the boundaries, even for a Fe-rich film, and is consistent with previous studies [39]. This result supports the notion that higher mobility atoms can segregate to the grain boundaries and contribute to the compositional dependent stress behavior. The segregation of the higher mobility atoms to the grain boundaries, even in films with overall enriched low mobility atom compositions, can contribute to controlling the stress state as a function of composition. Similar to Pt, the higher mobility of Cu provided a similar effect in regulating the intrinsic tensile growth stress of Fe. Thus, the  $\mu_c$  can be decreased with increasing composition of the higher mobile species (Pt or Cu) and the films can become more compressive according to the modified addition to Chason's model [10].

A cross-over point of 'zero' stress can be achieved between the tensile and compressive states of the film. This provides a means to tune in a desired stress within a film. This 'zero' state represents a balance between the adatoms moving to the boundaries and those growing vertically off the surface. The result of this balanced state provides for a smoother film surface, as evident by the AFM results. Trajectory aberrations in the atom maps that reveal the grain boundaries are a result of compositional fluctuations, density variations and/or surface modifications [41-43]. The visual appearances of grain boundaries for the Fe<sub>54</sub>Pt<sub>46</sub> and Pt films is a result of local density variations, as shown with the iso-density contour map which follows closely the grain boundaries by comparing figure 3.6(a) and (c) and figure 3.6(f) and (g). This provides experimental evidence that the film, which is in compression, is a result of an increase in atoms density at the grain boundary. For the zero stress Fe<sub>65</sub>Pt<sub>35</sub> film, the atom map shows little to no

trajectory aberrations, indicative of little to no compositional, density or surface variations across the boundaries. The compositional profile that spans the entire atom map would, on average, intersect approximately 10 grains or 20 grain boundaries (one on each side) based on the TEM/XRD determined grain sizes and field of view atom map collected. The composition profile, figure 3.6(e), shows no significant compositional variation.

In addition, the film surface is very smooth as quantified by AFM, i.e. no grain boundary grooving. Local grooving would result in a local curvature change and facilitate another contribution to a trajectory aberration during field evaporation. A deviation from 'zero' stress results in an increase in roughness. This roughness is likely a result in how the grain boundaries converge because of their intrinsic adatom mobility and resulting stress state. The AFM and atom maps are self consistent with each other. The difficulty to distinguish grain boundaries in the elemental Fe, as compared to Pt, is a result that the Fe film has a very similar roughness as the 'zero' stress film. Though the  $\text{Fe}_{54}\text{Pt}_{46}$  also has a similar roughness, as seen in figure 3.5, it has compositional variation at the boundaries, figure 3.6(b), that reveal the trajectory aberrations. Obviously, a compositional fluctuation would not exist in an elemental Fe film. As the films approached a 'zero' stress state, the films' surface was smoother, indicative of a balance in adatom mobility on the surface and to the grain boundaries.

Similar to Fe-Pt, the Fe-Cu film's atom map, figure 3.12, at the 'zero' stress condition does not show any significant compositional variation. This further supports that the lack of compositional segregation at the boundaries promotes a 'zero' stress condition, *e.g.* a balance of atomic species between one that is tensile promoting and the other compressive promoting. The compositional segregation of either the tensile or compressive stress state generating element at the grain boundaries or other types of interfaces is necessary to alter the stress condition towards

the enriching species' preferred stress state. Though the Fe-Cu system was a near equi-atomic balance for a 'zero' stress, the overall composition is not necessarily the predictive means for the film stress condition. The Fe-Pt system demonstrated that an overall enriched composition of one species does not dictate the stress condition, e.g. Fe is tensile stress promoting but the Fe<sub>54</sub>Pt<sub>46</sub> film was still compressive because of the Pt enrichment at the grain boundary.

The stress evolution after deposition for the Fe-Pt and Fe-Cu systems is depicted on figure 3.14. The stress behavior in the Fe-Pt system did not reveal a significant change (or recovery) upon ceasing the growth of the film. It has been noted in other systems, like Ag [9,10], the compressive stress can relax upon stopping the growth of the film. Chason *et al.* [10] has described this recovery in terms of a change in the surface chemical potential,  $\delta\mu_s$ , described previously. The lack of a stress change upon ceasing the growth suggests that the surface chemical potential between a condition of deposition and non-deposition is minor, these atoms do not have sufficient thermal mobility in the as-deposited condition for recovery, and/or the lack of a compressive state condition, for the zero stress state films, does not bias the atoms to migrate out of the boundaries. Koch *et al.* [21] have reported a recovery of elemental Fe's stress state at elevated temperatures suggesting Fe has limited mobility at room temperature. In general, the Fe-Cu system exhibited similar non-recovery behavior upon ceasing the deposition. The exception was elemental Cu, which did experience ~100 MPa change in stress after 250 s. This recovery of Cu has been reported by others [8] and indicates that Cu has some mobility for an ambient temperature deposited film. The preservation of a stress state for these alloyed films, even after deposition, provides the ability to retain the stress condition and potentially tune these films' mechanical behavior and failure modes at room temperature.

### 3.3. Conclusions

A series of 40 nm Fe-Pt and Fe-Cu thin films have been magnetron sputter-deposited onto Si [001] substrates. The *in situ* stress evolution of Fe, Pt, Cu and alloys of Fe-Pt and Fe-Cu thin films has been measured. It was found that the intrinsic stress state could be tuned to be either tensile, zero or compressive depending upon composition and deposition rate for similar grain sizes. The Cu and Pt elements were found to be the more mobile atoms as compared to Fe. The films near a 'zero' stress state were smoother and found to show little to no compositional segregation of one species enriching the boundary as compared to the bulk of the grain. We have provided a modified version of Chason *et al.*'s [10] thin film growth model to include a chemical potential term for the preferential segregation of one species to the grain boundaries. This has been used to describe how the stress state can be varied in a multi-component system. Finally, these intrinsic stress states of the alloy films studied appear to be retained, even upon ceasing deposition at ambient temperature.

## CHAPTER 4

### STRESS EVOLUTION DURING ORDERING

The FePt thin films have been extensively studied because its  $L1_0$  ordered phase has a large uniaxial magnetic anisotropy, up to  $10^8$  erg/cm<sup>3</sup>, which makes it a potential for next generation magnetic recording media [44]. However, the FePt thin films grown at room temperature are in A1 disordered, which is soft magnetic. In order to obtain ordered  $L1_0$  FePt phase, post annealing must be exerted [45]. During this annealing process, a large stress transition in FePt thin films has been demonstrated and it is believed that the transition is related to the changes in the fcc structure prior to  $L1_0$  phase transformation [46, 47]. In order to understand how the presence of the  $L1_0$  phase affects the stress evolution and relaxation, the Fe<sub>54</sub>Pt<sub>46</sub> thin films were grown at various elevated temperatures, the *in situ* stress evolution and post annealing stress relaxation were monitored, using wafer curvature measurement technique. XRD was used to characterize the structural information and correlate to the stress evolution. The magnetic properties of these thin films were measured with AGM.

#### 4.1. Experimental results

The series of 40 nm Fe<sub>54</sub>Pt<sub>46</sub> thin films were deposited at the ambient temperature of 25°C, and the elevated temperatures of 205 °C, 234 °C, 262 °C and 326 °C. After deposition, the thin films were held at the same temperature for approximately one hour to measure the post-growth compressive stress relaxation. The *in situ* stress evolution and the stress relaxation are plotted in figure 4.1. As the deposition temperature increased, the magnitude of the *in situ*

compressive stress decreased or, alternatively, the films' stress state moved towards the tensile stress state condition. In addition, the stress relaxation rate increased with increasing deposition temperature. Interestingly, the  $\text{Fe}_{54}\text{Pt}_{46}$  thin film stress is quite different from its elemental thin film components. The *in situ* stress evolution and post growth compressive stress relaxation of the Fe thin film at the three different substrate temperatures is plotted in figure 4.2(a) and (b). The Fe stress changes from a tensile state to a compressive state with increasing *in situ* deposition temperature. These results are consistent with the literature [21]. Once a compressive stress state is achieved, the magnitude of the stress relaxation does not change significantly with increasing substrate temperature over the range studied. However, for the elemental Pt thin film, the magnitude of the film's compressive stress becomes less compressive as temperature increases, figure 4.2(c). Interestingly, the less compressive the Pt film is, the larger degree of stress relaxation is observed at elevated temperature.

To correlate the stress state with the structure, XRD of these thin films was conducted. The ambient 25 °C and 205 °C films did not indicate the presence of any super-lattice reflections and were indexed as the A1 phase, figure 4.3(a). As the substrate temperature was increased to 235 °C, 260 °C and 325 °C, the XRD spectra could be consistently indexed to the  $L1_0$  phase. As the deposition temperature increased, the degree of  $L1_0$  order increased, as plotted in figure 4.3(b). This is consistent with the AGM results depicted in Figure 4.4.

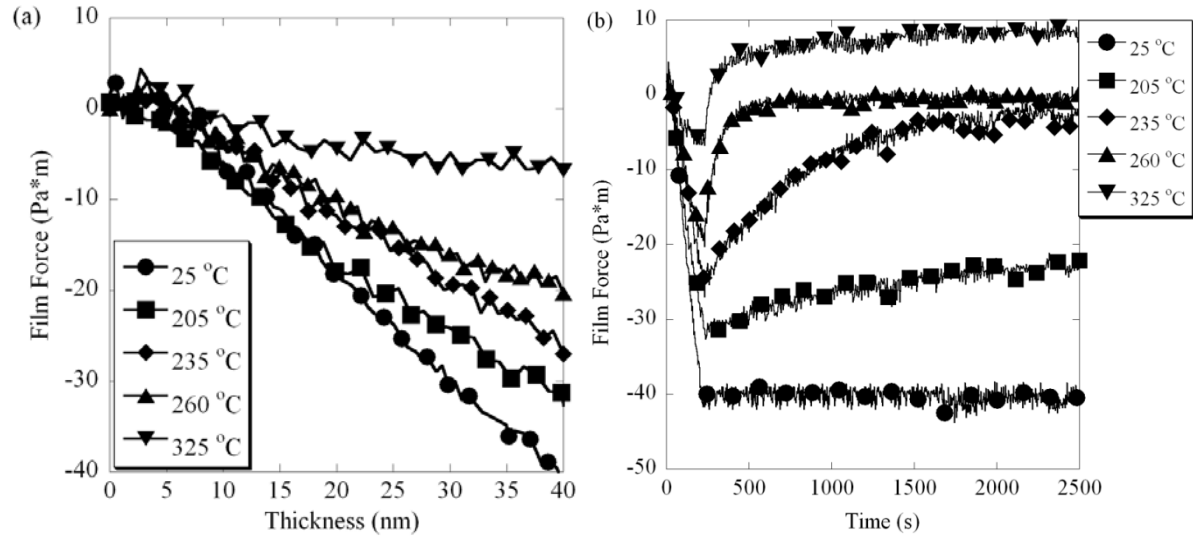


**Figure 4.1:** (a) Evolution of growth stresses for the Fe<sub>54</sub>Pt<sub>46</sub> thin films deposited at different substrate temperatures (b) Evolution of the growth stresses and the stress relaxation of Fe<sub>54</sub>Pt<sub>46</sub> thin films at different substrate temperatures.

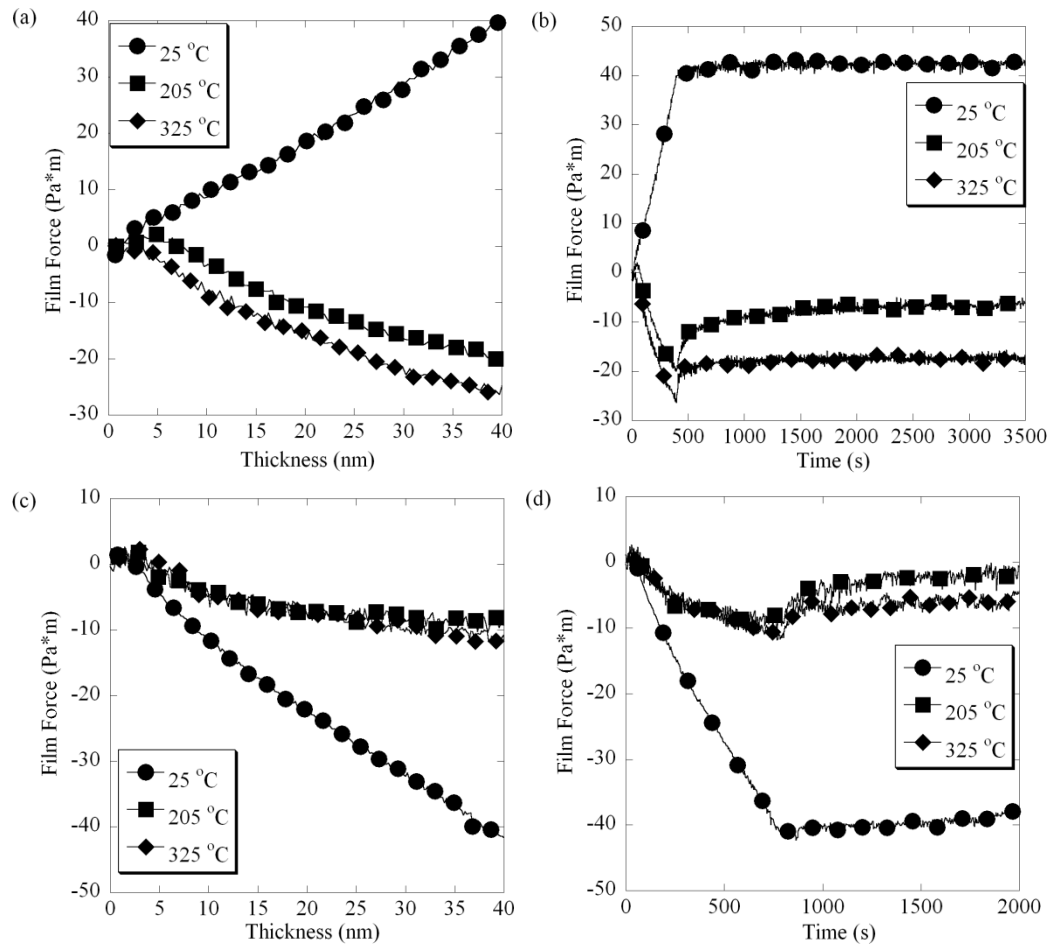


**Figure 4.2:** (a) Evolution of growth stresses of pure Fe thin films deposited at different substrate temperatures (b) Evolution of the growth stresses and the stress relaxation of the Fe thin films at different substrate temperatures (c) Evolution of growth stresses of pure Pt thin films deposited at different substrate temperatures (d) Evolution of the growth stresses and the stress relaxation of the Pt thin films at different substrate temperatures.

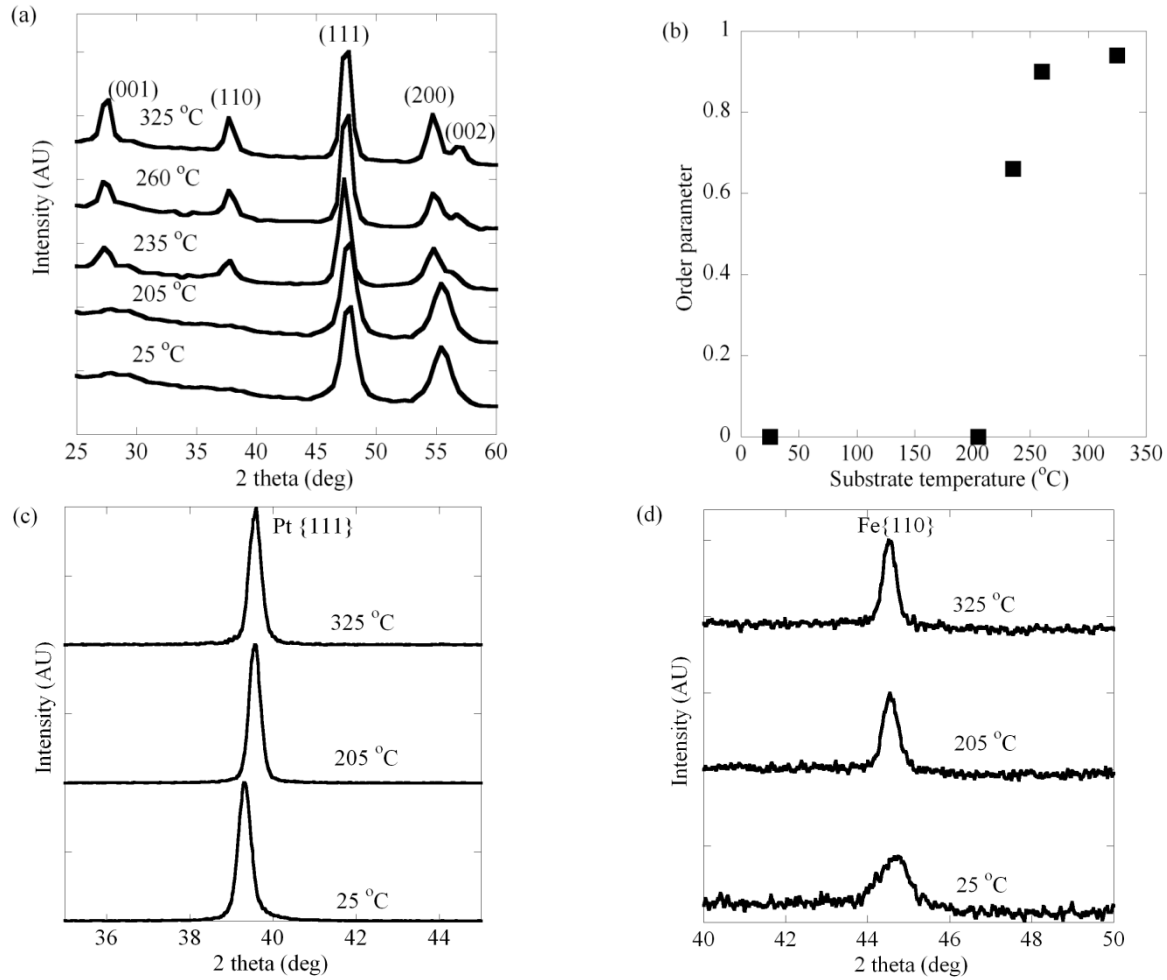


**Figure 4.3:** (a) XRD spectra using Co K $\alpha$  radiation titled at 35° chi for the Fe<sub>54</sub>Pt<sub>46</sub> thin films grown at different temperatures (b) Calculated order parameters for Fe<sub>54</sub>Pt<sub>46</sub> thin films grown at the different substrate temperatures (c) XRD spectra using Cu K $\alpha$  radiation for Pt thin films grown at different temperatures (d) XRD spectra using Cu K $\alpha$  radiation for Fe thin films grown at different temperatures.

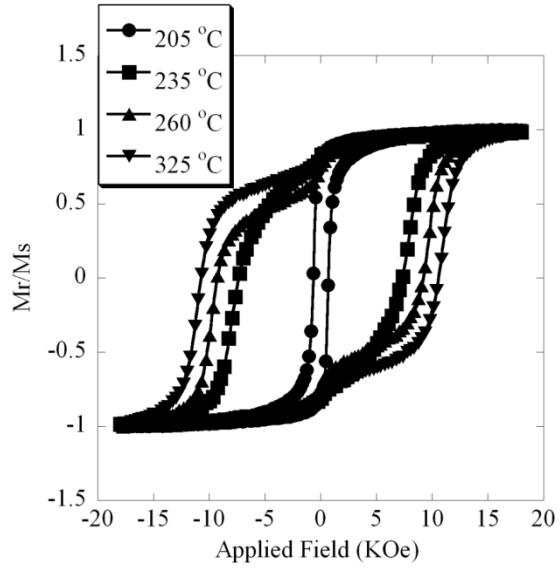


**Figure 4.4:** AGM results of the the  $\text{Fe}_{54}\text{Pt}_{46}$  thin films grown at different temperatures.

## 4.2. Discussions

Previous *ex situ* studies of FePt have shown that the phase transformation from A1 to  $L1_0$  results in a lower compressive state [46, 47]. The *in situ* ordering growth stress states are consistent with these *ex situ* results. The *in situ* studies revealed that the  $L1_0$  ordering temperature was lower than that reported for the *ex situ* anneals [48, 49]. This is a result of the added surface diffusivity that exists during growth [50, 51]. The  $L1_0$  phase transformation is a polymorphic transformation and does not require long-range atomic transport [52]. Thus, during growth the intrinsic increase in adatom mobility because of the arrival energies during deposition [50, 51] and free surface would be sufficient for increasing the short range diffusion necessary to order. In contrast, FePt  $L1_0$  ordering for *ex situ* anneals require a critical concentration of defects, such as vacancies, in the bulk to facilitate the diffusion-driven ordering processes. Consequently, for *ex situ* anneals, FePt  $L1_0$  ordering is a discontinuous precipitation event that initiates at the grain boundaries [49]. Grain boundaries are sources and sinks for vacancy migration and provide the necessary critical concentration of vacancies needed for atomic rearrangement [53]. As reported by Torres and Thompson [39], a reduction in Pt concentration at grain boundaries occurs during the ordering process of the FePt thin films. This reduction of Pt-enrichment, a larger atom than Fe, at the grain boundaries will lead to the decrease in compressive stress. In the *ex situ* anneals, Wieman *et al.* [46,47] suggested that a reduction of stress occurs before ordering because of a structural changes in the disordered fcc phase as evident by the shift of the  $\{111\}$  peaks towards a lower angle. The migration of Pt from the boundaries prior to significant superlattice reflections, as shown by Torres and Thompson [39], could be the experimental rationalize of that stress observation. In the *in situ* stress behavior, the stress at elevated temperatures is a

continuously varying function suggesting that ordering, and any possible structural rearrangements, such as Pt enrichment at boundaries, as seen with *ex situ* anneals does not occur.

As the film becomes more ordered (higher deposition temperature) during growth, the magnitude of compressive stress is reduced, figure 4.1(a). Chason *et al* [10] has suggested that the compressive stress during ordering is a result of adatoms migrating to the coalesced grain boundaries because of a chemical potential driving force difference between the growth surface and the grain boundaries. Clearly, the change into an ordered phase inhibits the mobility of Fe or Pt atoms on the surface to diffuse to the boundaries. These atoms likely become ‘locally bonded’ to a preferred lattice sites on the surface that places Fe or Pt into the correct coordination environment for  $L1_0$ , as schematically shown in figure 4.5(a). Hence, ordered surfaces, by the nature of the atomic positional order, could ‘anchor’ atoms thus limiting surface mobility.

In addition, the chemical nature of the grain boundaries changes between a disordered and ordered condition. A grain boundary, by definition, is an interface formed by two non-aligned crystalline materials. For a grain boundary formed from two disordered phases, free volume and a local coordination change will exist for atoms within the boundary. Similarly, a free volume and coordination change would exist with the impingement of two chemically ordered grains. The nature that specific atoms are in specific sites for each ordered grain would provide an additional energy penalty when the two grains impinge because the atoms on either side of the boundary are ordered. This would be analogous to an anti-phase boundary, except a grain boundary is not a stacking fault. The migration of an adatom to a boundary formed by two ordered phases will experience an additional asymmetric chemical environment, as compared to a disordered impingement of grains, as illustrated in figure 4.5(b). Consequently, this chemical distinction across the boundary leads to an additional increase in chemical potential for either a

Pt or Fe atom that has migrated into the boundary during growth. The ceasing of the deposition lowers the surface chemical potential and the atoms quickly migrate out of this boundary because of this additional chemical energy contribution to the driving force. The increase in atom migration out of the boundaries, even to a tensile state for the highest annealed film, is clearly evident by the increasing stress relaxation rate with increasing order parameter. The temperature difference over this range was less than 100°C between the disordered and ordered states. Thus there is not a larger thermal assisted component for migration out of the boundaries between the films. Note that the disordered and partially ordered films have initially a higher magnitude of compressive stress, *e.g.* a greater bias for stress relaxation. The latter comment indicates that the magnitude of compressive stress is not sufficient to determine the rate of stress relaxation. Even for the 235 °C Fe<sub>54</sub>Pt<sub>46</sub> film, where  $S \approx 0.6$ , the stress relaxation rate increased substantially as compared to the disordered film at 205 °C, just a  $\Delta T = 30$  °C lower in temperature. Clearly, the higher the order parameter, the more important role the chemical component will play in the grain boundary's chemical potential. Once the atoms are on the surface, they can surface diffuse and coordinate their bonding to an 'ideal' site which matches the chemical order arrangement for that lattice (grain) direction. Obviously, this explanation does not assume surface energy conditions which can disorder an ordered surface. Recent modeling predictions have shown that surface disordering is not significant in a highly ordered FePt surface in an ideal vacuum [54], which would be the approximate case in the deposition chamber.

In terms of the elemental films, as the deposition temperature increased, the elemental Fe became more compressive. This is a result of the thermal assisted mobility of the Fe adatoms on the surface [21]. The reduction of the compressive state for pure Pt thin films is not well understood but is likely a result of a stress-induced structural change as evident in the shift of the

Pt {111} peaks plotted figure 4.3(c). The Pt film experiences a slightly smaller lattice parameter, which is equivalent to a smaller atomic volume hence reduced compression at the boundaries. The origin of this change, for an element metal, is the subject of future work.

#### 4.3. Conclusion

As a  $\text{Fe}_{54}\text{Pt}_{46}$  thin film orders *in situ* during growth, the magnitude of the compressive stress state is reduced. The compressive stress relaxation rate is increased with increasing substrate temperature or order parameter. The extent of stress relaxation is significantly different than that of elemental Fe or Pt thin films. The compressive stress reduction, for the ordered  $\text{Fe}_{54}\text{Pt}_{46}$  films, has been rationalized as a reduction of adatom mobility on the surface as Fe and Pt occupy specific lattice sites for  $L1_0$  on each grain. In addition, the ordered nature of the grains contributes to additional chemical energy at the boundary which, upon ceasing deposition, significantly increases the relaxation rate, even to a condition of being tensile for the highest deposition temperature of 325 °C. The *in situ* deposition temperatures ordered the films at a lower temperature as compared to previous reports in the literature [48, 49].

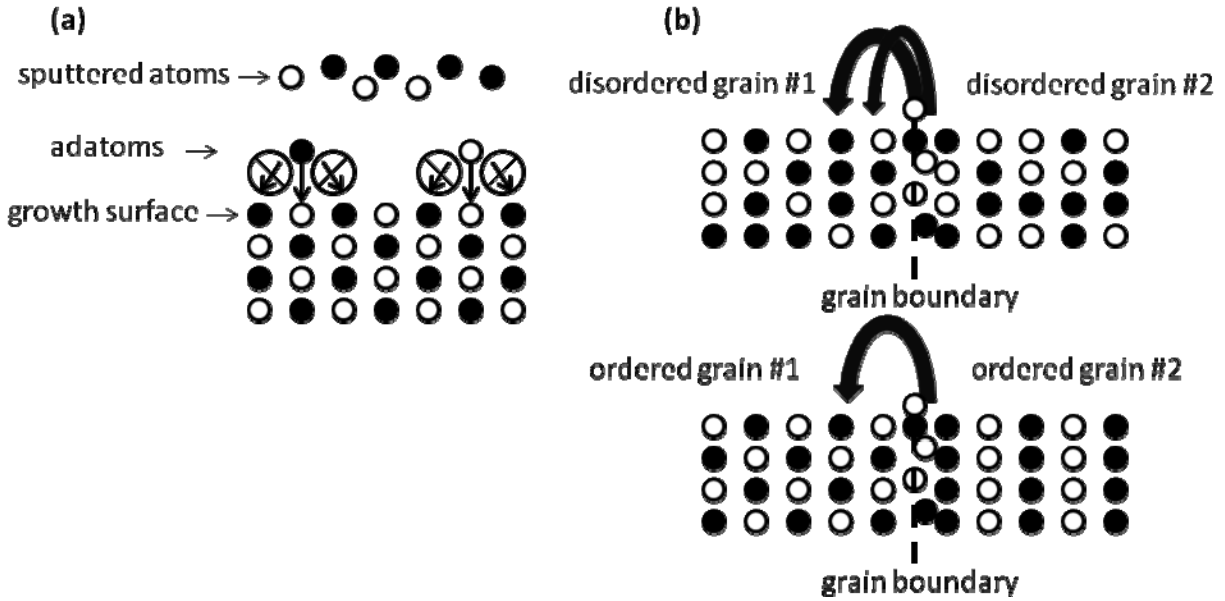


**Figure 4.5:** (a) Illustration of preferred lattice site attachment of adatoms onto an ordered surface during growth. (b) Upon ceasing the deposition, compressive stress relaxation can occur as atoms migrate out of the boundary. The top illustration is a boundary formed from two disordered grains. The bottom illustration is a boundary formed from two ordered grains at two different orientations. The accommodation of atoms in a boundary between two ordered grains can provide additional chemical contributions to the migration of atoms out of the boundary because of the distinct chemical differences as compared to the impingement of two disordered grains, as illustrated. The arrows indicate that atoms, once on the surface, may bind to either type of atom in a disordered system (two arrow option) versus a specific atom in an ordered surface (one arrow option).

## CHAPTER 5

### STRESS EVOLUTION DURING PHASE SEPARATION

As was shown in previous chapter, the *in situ* stress evolution of  $\text{Fe}_x\text{Cu}_{100-x}$  alloy thin films is strongly dependent on its composition and affected by its deposition rates. However, if these  $\text{Fe}_x\text{Cu}_{100-x}$  alloy thin films are grown at elevated temperature, the Fe and Cu elements will become separated with each other and form two-phase metal films, whose microstructures are different from that grown at ambient temperature. This microstructure change will lead to different stress behavior.

In this chapter, three  $\text{Fe}_{51}\text{Cu}_{49}$  alloy thin films grown at various temperatures were taken to investigate how stress evolves during element separation with each other. The *in situ* stress evolution and post growth stress relaxation were measured and the microstructure of these thin films were also characterized to explore the mechanism of the stress evolution.

#### 5.1. Experimental Results & Discussion

The *in situ* stress evolution of the 40 nm  $\text{Fe}_{51}\text{Cu}_{49}$  film is plotted in figure 5.1(a). The generic compressive-tensile-compressive behavior [13] of the film is captured for each deposition temperature. Consequently, the films have developed similar microstructures during their initial nucleation and island growth stages. This is consistent with literature stating that the Fe and Cu elements do not separate during initial growth [55]. In general, increasing the deposition temperature resulted in an increase in the magnitude of the compressive stress during the continuous growth stage. Unlike the ambient temperature deposition, where the stress state appears near zero and constant after  $\sim 5$  nm of growth, the compressive state condition continues

to change with increasing thickness for the elevated temperatures. Upon ceasing the deposition, the stress relaxation, i.e. recovered compressive stress, can be monitored. For the ambient 25 °C and 325 °C films, the stress relaxation is very small as compared to the 205 °C film, as seen in figure 5.1(b).

The XRD results confirm that the as-deposited film at ambient temperature adopted a meta-stable solid solution phase as evident by the single face centered cubic (fcc) {111} peak and this result is consistent with a previous report [56]. This peak is in close agreement with the phase separated {111} peak of Cu, also shown in figure 5.2(a). Selected area electron diffraction (SAED), shown in figure 5.2(b), has multiple diffracted rings which confirmed the fcc symmetry. As the temperature increased, the {111} Cu peak was retained along with the appearance of the {002} Cu peak. At elevated temperatures, the phase separation of the body centered cubic (bcc) Fe phase was also evident by the XRD {011} and {002} peaks in figure 5.2(a). This phase separation is consistent with the literature reports [55,57,58].

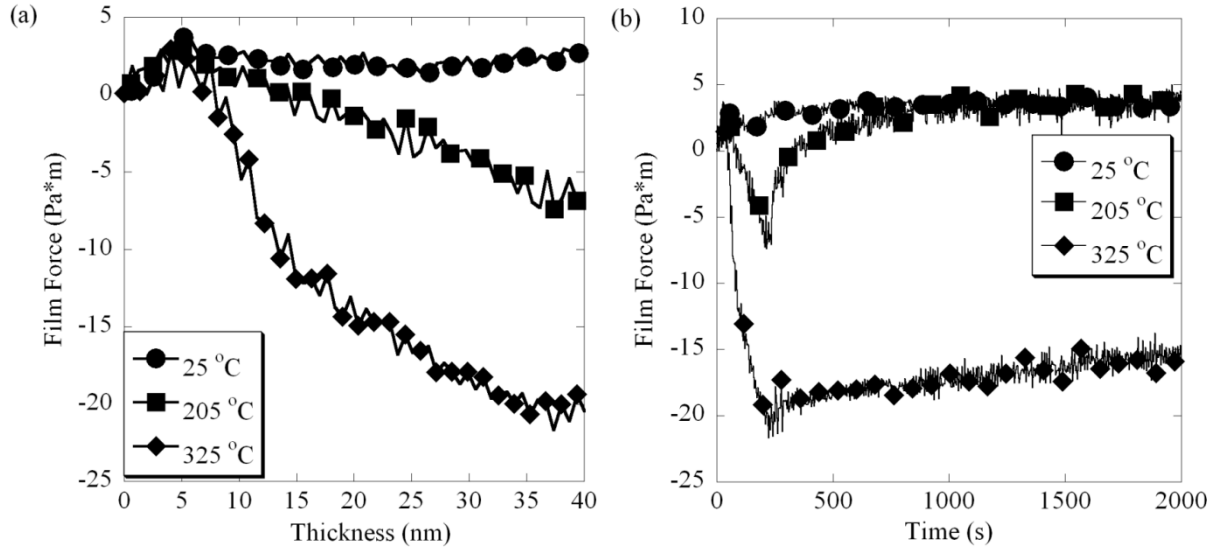


**Figure 5.1:** (a) Evolution of growth stresses of the Fe<sub>51</sub>Cu<sub>49</sub> thin films deposited at different substrate temperatures; (b) the evolution of the growth stresses and the stress relaxation of Fe<sub>51</sub>Cu<sub>49</sub> thin films at different substrate temperatures.

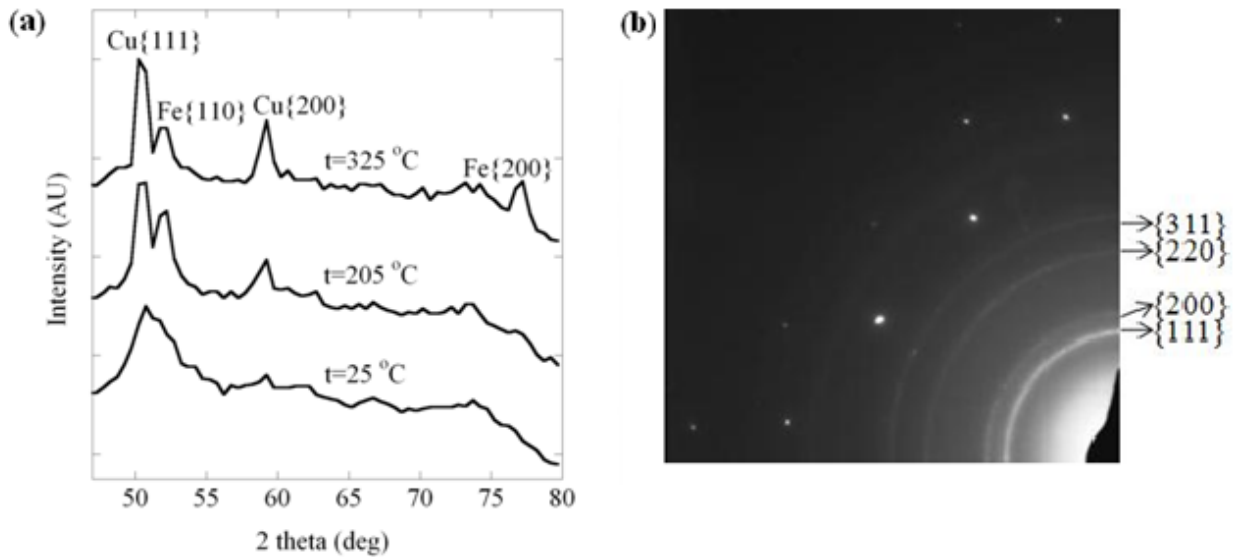


**Figure 5.2:** (a) XRD profiles of the Fe<sub>51</sub>Cu<sub>49</sub> thin films grown at different temperatures using Cu K $\alpha$  X-rays; (b) TEM selected area diffraction pattern of the Fe<sub>51</sub>Cu<sub>49</sub> thin films grown at ambient temperature shows a fcc symmetry.

The increase in compressive stress with increasing growth temperature is a result of increasing adatom mobility [21]. Particularly in the Fe-Cu system, there is a strong tendency for Cu segregation to grain boundaries [59]. At ambient temperatures, where the adatom mobility is low, such an effect leads to a relatively smaller percentage of one species of atoms segregated to the grain boundaries. As a consequence, a stress near ‘zero’ can be achieved by balancing species which favor either tensile, as reported for Fe [11], or compressive growth, as for Cu [8], as evident in figure 5.1(a). However, at elevated temperatures, the Cu and Fe adatom mobility is increased facilitating the thermodynamically favorable phase separation because of immiscibility. Begrambekov *et al.* [55] have inferred that the Fe islands nucleate off of the Cu islands during growth. This is consistent with the results presented here, *e.g.* the ambient temperature phase is fcc with the bcc phase forms at elevated temperatures as seen in the XRD spectra of figure 5.2(a). The STEM-High Angle Annular Dark Field (HAADF) micrographs of figure 5.3 for the elevated temperature deposits appear to indicate that the Cu, the brighter phase, encases the Fe, the lower contrast phase. Note that the HAADF image is formed from incoherently scattered electrons that are sensitive to the atomic number [60]; thus brighter regions represent higher atomic number elements. The micrograph, at 325 °C, clearly shows the faceting of the bcc Fe surrounded by the fcc Cu matrix. It is interesting to note that the elevated temperature deposits retain a compressive nature in the film upon phase separation. Both Fe and Cu have equivalent atomic volumes of 0.7 nm<sup>3</sup>. A change in atomic volume, either smaller or larger than the matrix phase, should facilitate a mechanical response of the entire film to the phase transformation. Since both elements are equivalent, the retention of a compressed state could be associated with either the preferential diffusion of Cu to the boundaries [59] and/or differences in thermal expansion, *i.e.*  $\alpha_{\text{Cu}} > \alpha_{\text{Fe}}$ . Kőszegi and Somogyvári [61] have reported

thermal expansion variations as a function of stress state in the precipitation of Cu in a Fe-rich alloy.

The 25 °C and 325 °C deposited films, though microstructurally different in that the former film is a solid solution and the latter is phase separated, exhibited near equivalent magnitudes in stress relaxation, figure 5.1(b). In contrast, the 205 °C film, which had diffraction evidence of phase separation, exhibited a rapid stress recovery. Chason *et al* [10] has proposed that the compressive force observed post-tensile stress is a result of adatoms being driven to the coalesced grain boundaries because of the chemical potential difference between the growth surface and the grain boundaries. Upon ceasing the deposition, the surface chemical potential changes which can allow for the migration of atoms out of the grain boundaries relieving the compressive stresses [10].

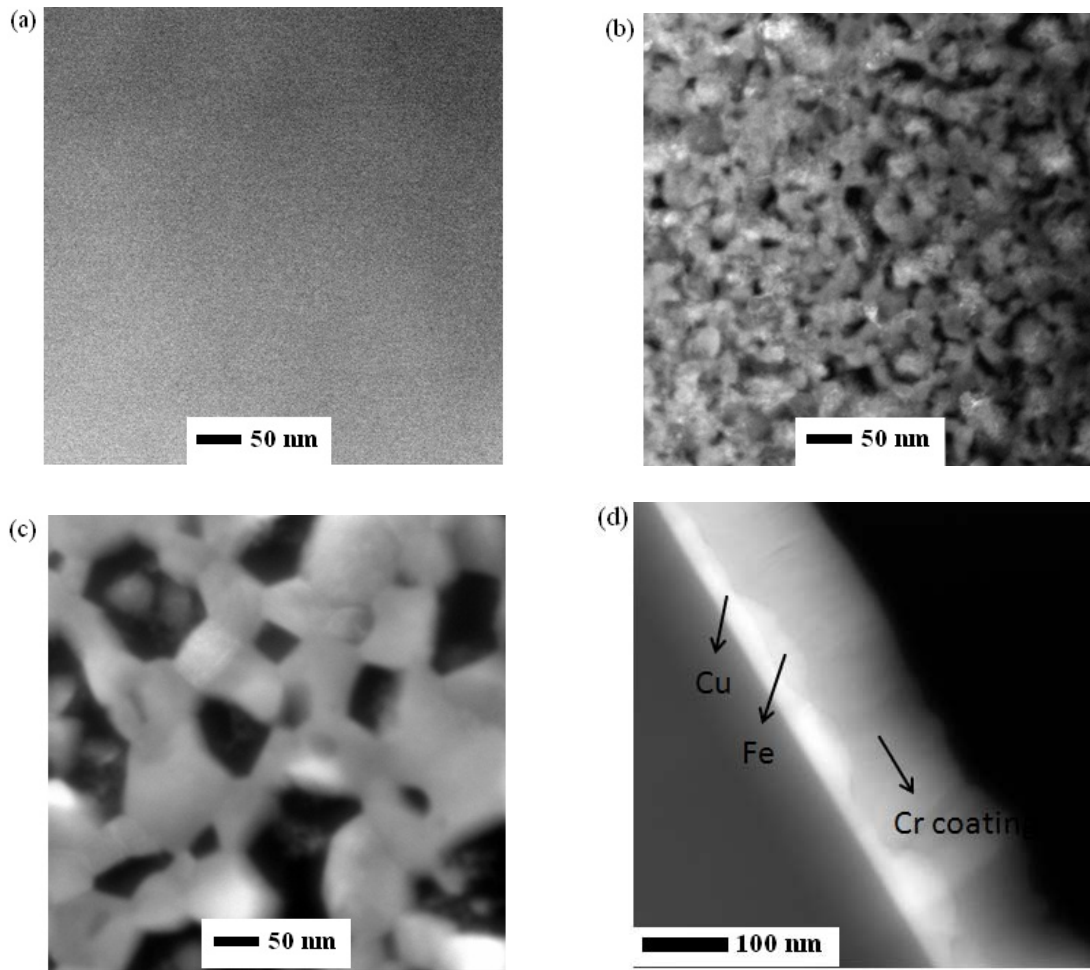


**Figure 5.3:** TEM-HAADF plane-view images of the the  $\text{Fe}_{51}\text{Cu}_{49}$  thin films grown at ambient temperature (a), 205 °C (b), and 325 °C (c) respectively. (d) TEM cross-section HAADF image of the  $\text{Fe}_{51}\text{Cu}_{49}$  thin films grown at 325 °C.

The ambient temperature deposited film has negligible phase separation, evident in the mono-contrast in the STEM-HAADF image of figure 5.3(a) and solid solution fcc reflections in figure 5.2(a) and (b). The lack of phase separation, *i.e.* the creation of chemically distinct boundaries, and low deposition temperature indicates insufficient atomic mobility. Consequently, the arrival of Fe or Cu adatoms during deposition and their subsequent migration into the boundaries that are formed by chemically disordered grains does not provide a sufficient thermodynamic driving force or thermal assisted mobility to drive those same atoms out of the boundaries upon ceasing the deposition. Additionally, the near ‘zero’ stress state for the 25 °C deposited film does not have a compressive force to bias the migration of atoms out of the boundaries. Thus the lack of stress recovery suggests that either the chemical potential does not significantly change upon ceasing deposition and/or there is insufficient compression force present for relaxation. In contrast, the 325°C sample is in a compressive stress state and has sufficient thermal energy for mobility. The lack of a rapid stress relaxation is likely a result that the atoms have already segregated and coarsened to the thermodynamic preferred phase during growth and are not significantly driven out of the boundaries. As stated previously, the retained compressive force could be a result of either thermal expansion differences [61]. The plan-view STEM-HAADF image, figure 5.3(c) and the cross-section STEM-HAADF in figure 5.3(d), clearly shows phase separation in- and out-(vertical) to the growth plane.

The significant post-growth stress relaxation of the 205 °C film suggests that the atoms have not fully phase separated or coarsened thus they are driven out from the boundaries because of the change in chemical potential upon ceasing the deposition. A comparison the STEM-HAADF images for the 205 °C and 325 °C deposited temperatures in figure 5.3 clearly reveal that the lower temperature film has not coarsened (phase separated) as much as the higher

temperature deposited film. Upon ceasing the deposition at 205 °C, excess Fe or Cu atoms have sufficient thermal mobility and a compressive stress state to migrate out of the grain boundaries, thereby reducing the compressive stress. These atoms then surface diffuse towards a surface of a thermodynamically favorable phase, as schematically shown in figure 5.4(a). Over time, the migration of atoms to these surfaces, wither during growth or post-growth stress relaxation, would lead to roughening, as schematically shown in figure 5.4(b). The atoms on the planar surface will coalesce together to minimize surface area while maximizing volume on the planar surface, which is similar to Strankski-Krastanov growth [2]. The AFM images, figure 5.5, clearly reveal enhanced surface roughening with increasing deposition temperature, *e.g.* phase separation. It is peculiar that the 205 °C deposit, which has a lower compressive stress state thereby a lower bias for stress relaxation as compared to the 325 °C deposit, would exhibit such a significantly higher stress relaxation rate. This indicates that the microstructure of phase separation during growth likely is a significant contributor to the differences observed.

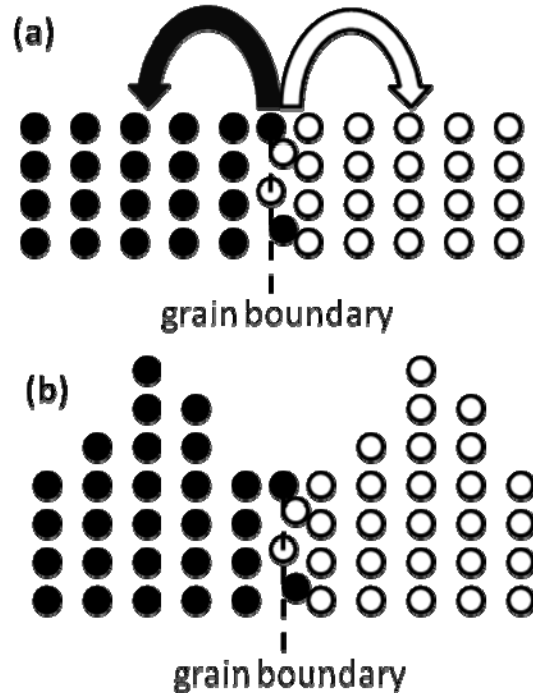


**Figure 5.4:** A schematic description about atom movement during phase separation.

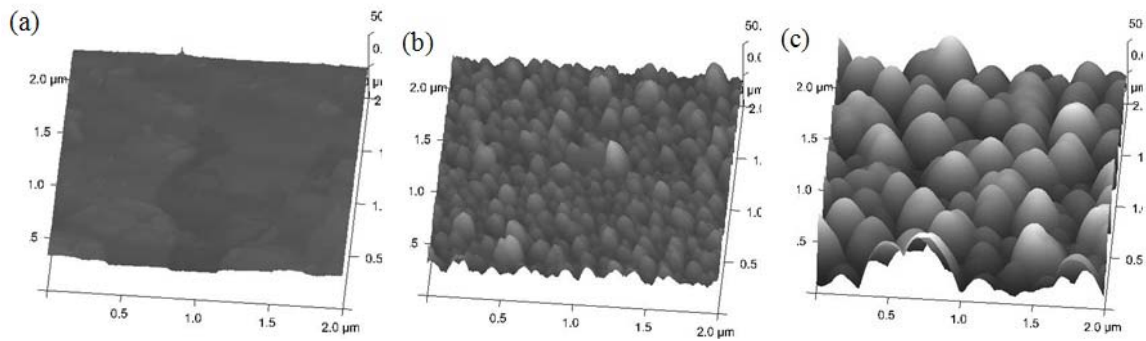


**Figure 5.5:** AFM images of the the the Fe<sub>51</sub>Cu<sub>49</sub> thin films grown at ambient temperature (a), 205 °C (b), and 325 °C (c), the roughness are 1.3 nm, 5.4 nm and 15.7 nm.

## 5.2. Conclusions

Three Fe<sub>51</sub>Cu<sub>49</sub> thin films have been magnetron sputter-deposited onto a Si<sub>3</sub>N<sub>4</sub> underlayer film with a [001] Si substrate. The *in situ* growth stress and post-growth stress relaxation has been measured and their microstructures have been characterized. The *in situ* growth stresses were found similar in the initial island nucleation and island growth regions while the compressive stress in the continuous growth regime increased with substrate temperature. Increasing the deposition temperature resulted in a coarser phase separated microstructure and rougher surface topology. This has been rationalized as the migration of adatoms to thermodynamically preferred surfaces during growth. The post-growth stress relaxation of the sample at ambient temperature is small, indicative of either limited atom mobility or insignificant compressive mechanical driving forces because the film was in a near ‘zero’ stress state. The sample grown at 205 °C relaxed rapidly upon ceasing deposition. This relaxation at this temperature was sufficient to drive excessive atoms out of at grain boundaries towards preferable phase surfaces. For the film grown at 325 °C, the film retained its larger compressive stress condition, likely because of thermal expansion differences and favorable migration of Cu atoms to grain boundaries as reported in the literature [59]. This film experienced a negligible stress relaxation after deposition and believed to be a result that during growth the atoms had sufficient mobility to grow onto their respective phase surfaces which led to enhanced roughening.

## CHAPTER 6

### CONCLUSIONS AND FUTURE WORK

The *in situ* and post growth stress evolution of the Fe-Pt and Fe-Cu alloy systems was studied and correlated to the microstructure evolution. At ambient temperature and constant deposition pressure, the growth stresses of both the Fe-Pt and Fe-Cu alloy were found to be dependent on the compositions. The final intrinsic stress state after growth could be tuned to be either tensile, zero or compressive depending upon composition and deposition rate for similar grain sizes. This is because of preferential segregation of one species (the more mobile element) to the grain boundaries.

At elevated growth temperatures, the near equiatomic FePt alloy forms an ordered  $L1_0$  phase while the equiatomic FeCu alloy phase separates. The magnitude of the compressive stress state is reduced as the  $\text{Fe}_{54}\text{Pt}_{46}$  thin film orders *in situ* during growth. The compressive stress relaxation rate is increased with increasing substrate temperature or order parameter. This compressive stress reduction has been rationalized as a reduction of adatom mobility on the surface as Fe and Pt occupy specific lattice sites for  $L1_0$  on each grain. The ordered nature of the grains contributes to additional chemical energy at the boundary which, upon ceasing deposition, significantly increases the relaxation rate. In contrast, the growth compressive stress of the  $\text{Fe}_{51}\text{Cu}_{49}$  alloys in the continuous growth regime increased with substrate temperature. This has been rationalized as the migration of adatoms to thermodynamically preferred surfaces during growth.

In this work, the composition dependent stress evolution and stress evolution during *in situ* ordering and phase separation was studied. However, the following issues are recommended for future work:

1. The mechanism of compositional dependent stress is not yet fully understood. A model can be constructed to simulate the process and uncover the compositional dependent stress mechanism(s) and how different residual stresses affect the attachment of the thin film to the substrate.
2. The growth stress of the  $\text{Fe}_{51}\text{Cu}_{49}$  alloy during *in situ* phase separation was found to be compressive. However, the atomic volume of Fe and Cu are about the same. An interesting study would be how the stress evolution changes during the phase separation of two elements with very distinct atomic volumes.
3. The growth stress of  $\text{Fe}_{54}\text{Pt}_{46}$  during *in situ* ordering and  $\text{Fe}_{51}\text{Cu}_{49}$  during *in situ* phase separation was studied. Another interesting study would be how the results compare to *ex situ* ordering and phase separations, since both the *in situ* ordering and phase separation temperature is much lower than *ex situ*. The role of adatom mobility during growth in phase transformation and how phase transformations change the mobility of atoms during growth offer ample opportunities of further investigation as a function of the strength on the thermodynamic mixing term.

## Reference

1. Donald Smith, *Thin film Deposition: Principles and practice*, McGraw-Hill Professional, p. 1-7 (1995).
2. Donald Smith, *Thin film Deposition: Principles and practice*, McGraw-Hill Professional, p. 119-221 (1995).
3. J. Barbosa, B. Almeida , A.M. Pereira , J.P. Araújo, I. Gomes , and J. Mendes, *Journal of Non- Crystalline Solids* **354**, 5250 (2008) .
4. A. Miyamura, K. Kaneda, Y. Sato, and Y. Shigesato, *Thin Solid Films* **516**, 4603 (2008).
5. J. Zhu , Y.R. Li, Y. Zhang, X.Z. Liu, and B.W. Tao, *Ceramics International* **34**, 967 (2008).
6. C.T. Chuanga, C.K. Chaob, R.C. Changa, and K.Y. Chub, *J. Mater Proc Tech.* **201**,770 (2008).
7. R Koch, *J. Phys.: Condens. Matter* **6**, 9519 (1994).
8. M. Pletea, W. Bruckner, H. Wendrock, and R. Kaltofen, *J. Appl. Phys.* **97**, 054908 (2005).
9. R. Abermann and R. Koch, *Thin Solid Films* **129**, (71) 1985.
10. E. Chason, B. W. Sheldon, L. B. Freund, J. A. Floro and S. J. Hearne, *Phys. Rev. Lett.* **88**, 156103 (2002).
11. D. Sander, A. Enders, and J. Kirschner, *Appl. Phys. Lett.* **67**, 1833(1995).
12. M. Pletea, W. Bruckner, H. Wendrock, R. Kaltofen, and R. Koch, *J. Appl. Phys.* **99**, 033509 (2006).
13. R. C. Cammarata, T. M. Trimble, and D. J. Srolovitz, *J. Mater. Res.* **15**, 2648 (2000).
14. Jerrold A. Floro, Eric Chason, Robert C. Cammarata, and David J. Srolovitz, *MRS bulletin*, Jan (2002).
15. C. Friesen and C. V. Thompson, *Phys. Rev. Lett.* **89**, 126103 (2002).
16. C. Friesen, S. C. Seel and C. V. Thompson, *J. Appl. Phys.* **95**, 1011 (2004).
17. R. W. Hoffman, *Thin Solid Films* **34**, 185 (1976).
18. C. V. Thompson, *J. Mater. Res.* **14**, 3164 (1999).
19. W. D. Nix and B. M. Clemens, *J. Mater. Res.* **14**, 3467 (1999).
20. L. B. Freund and E. Chason, *J. Appl. Phys.* **89**, 4866 (2001).
21. R. Koch, Dongzhi Hu and A. K. Das, *Phys. Rev. Lett.* **94**, 146101 (2005).

22. Brian W. Sheldon, Adi Ditkowski, R. Beresford, Eric Chason, and Janet Rankin, *J. Appl. Phys.* **94**, 948 (2003).
23. Chun-wei Pao, Stephen M. Foiles, Edmund B. Webb, David J. Srolovitz and Jerrold A. Floro, *Phys. Rev. Lett.* **99**, 036102 (2007).
24. Cody Friesen and Carl V. Thompson, *Phys. Rev. Lett.* **95**, 229601 (2005).
25. R. Koch, Dongzhi Hu and A. K. Das, *Phys. Rev. Lett.* **95**, 229602 (2005).
26. A. Shull and F. Spaepen, *J. Appl. Phys.* **80**, 6243 (1996).
27. H. J. Schneeweis and R. Abermann, *Vacuum* **43**, 463 (1992).
28. G. Thurner and R. Abermann, *Thin Solid Films* **192**, 277 (1990).
29. D. Winau, R. Koch, A. Fuhrmann, and K.H. Rieder, *J. Appl. Phys.* **70**, 3081 (1991).
30. St. Bertel and R. Abermann, *Thin Solid Films* **473**, 1 (2005).
31. A. L. Del Vecchio and F. Spaepen, *J. Appl. Phys.* **101**, 63518 (2007).
32. D. Winau, R. Koch, and K. H. Rieder, *Appl. Phys. Lett.* **59**, 1072 (1991).
33. G. G. Stoney, *Proc. R. Soc. London, Ser.A* **82**, 172 (1909).
34. C. Taylor, D. Bartlett, E. Chason and J. Floro, *The Industrial Physicists* **4**, 25 (1998).
35. Peterson, *Proc. IEEE* **70**, 420 (1982).
36. Yuji Sasanuma, Mamoru Uchida, Kazuyuki Okada, Katsuhiko Yamamoto, Yukishige Kitano, and Akira Ishitani, *Thin Solid Films* **203**, 113(1991).
37. G. K. Williamson and W. H. Hall, *Acta Metall.* **1**, 22 (1953).
38. K. Thompson, D. Lawrence, D.J. Larson, J.D. Olson, T.F. Kelly, B. Gorman, *Ultramicroscopy* **107**, 131(2007).
39. K.L. Torres and G.B. Thompson, *Ultramicroscopy* **109**, 606 (2009).
40. C.-M. Kuo, P. C. Kuo, and H.-C. Wu, *J. Appl. Phys.* **85**, 2264(1999).
41. M.K. Miller, A. Cerezo, M.G. Hetherington, G.D.W. Smith, *Atom Probe Field Ion Microscopy*, Clarendon Press, Oxford, , p. 196 (1996).
42. M.K. Miller, M.G. Hetherington, *Surface Science* **246**, 332 (1991).
43. M. Thuvander, H.-O. Andre' n, *Materials Characterization* **44**, 87 (2000).

44. D. Weller, A. Moser, L. Folks, M.E. Best, W.E. Lee, M.F. Toney, M. Schwickert, J.-U. Thiele, M.F. Doerner, *IEEE Trans. Magn.* **36**, 10 (2000).
45. K. Coffey, M. A. Parker and J. K. Koward, *IEEE Trans. Magn.* **31**, 2737(1995).
46. K.W.Wierman, C.L.Platt, and J.K.Howard, *J. Appl.Phys.* **93** (2003),7160.
47. K.W.Wierman, C.L.Platt, and J.K.Howard, *Mat.Res.Symp.Proc.* **795**, U5.8.1 (2004).
48. Y.K.Takahashi, M.Ohnuma and K.Hono, *Jpn. J. Appl. Phys.* **40**, L1367 (2001).
49. Y.K.Takahashi, and K. Hono, *Scripta Materialia* **53**, 403(2005).
50. Ronald. R. Willey, *Practical Equipment, Materials, and Processes for Optical Thin Films* (1st ed), Willey Optical, Consultants, p.90-91 (2007).
51. Menghua Xia, Xu Liu, and Peifu Gu, *Applied Optics* **32**, (5443) 1993.
52. S.H. Whang, Q. Feng, and Y.Q. Gao, *Acta Mater* **46** , 6485(1998).
53. D.A. Porter and K.E. Easterling, *Phase Transformations in Metals and Alloys* (2nd ed.), Chapman & Hall, London p. 303-304 (1992).
54. R.V. Chepulskii, W.H. Butler,A. van de Walle, and Stefano curtarolo, *Scripta Mater.* (2009).
55. L. B. Begrambekov, A.A Gordeev, and Ya. A. Sadovshii, *Journal of Surface Investigation* **2**, 419 (2008).
56. A. R. Yavari, P. J. Desre, and T.B. Benameur, *Phys. Rev. Lett.* **68**, 2235 (1992).
57. J. Eckert, J. C. Holzer, and W. L. Johnson, *J. Appl. Phys.* **73**, 131 (1993).
58. K. Sumiyama, Y. Yoshitake, and Y. Nakamura, *Acta Metall* **33**, 1785 (1985).
59. E. D. Hondros, and M. P. Seah, in *Physical Metallurgy*, 3<sup>rd</sup> edition, edited by R. W. Cahn and P. Haasen (Elsevier Science,Amsterdam,1983), p.865.
60. David. B. Williams, and C. Barry. Carter, *Transmission Electron Microscopy*, Springer Science and Business Media Inc, p. 358-361 (1996).
61. L. Kőszegi , and Z. Somogyvári, *Physica B.* **276-278**,909 (2000).

62. T.B. Massalaki (editor), *Binary Alloy Phase Diagrams*, ASM International, Ohio, p.1752 (1990).
63. Max Hansen, and Kurt Anderko, *Constitution of Binary Alloys*, Genium Publishing Corporation (2<sup>nd</sup> edition), p581 (1958).

APPENDIX A

SUBTRACTION OF GROWTH STRESS FROM UNDER-LAYER AND THERMAL  
EXPANSION

In the studies of Chapter 4 and Chapter 5, the metallic thin films were grown on Si substrates with a  $\text{Si}_3\text{N}_4$  buried layer at elevated temperatures. Therefore, both the intrinsic stress from the metallic thin film layer and the buried layer and thermal expansion was measured by MOS, as shown in Figure A.1. The advantage of the MOS is that it can take any previous any measurement as its “zero” reference point. Both the stress from the  $\text{Si}_3\text{N}_4$  buried layer and the thermal stress due to different thermal expansion coefficients of the substrate and the thin films were subtracted and only the intrinsic stress of the metallic thin film layer were counted, Figure A.2.

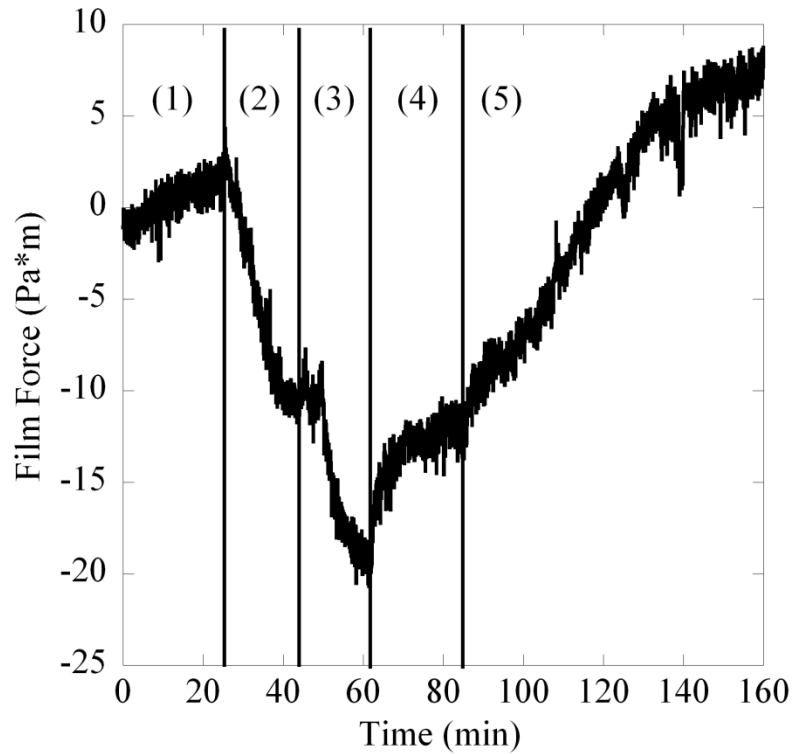


**Figure A.1:** Original stress measurements of pure Pt thin films with 10nm buried layer grown at 205°C with a deposition rate of 0.05 nm/s. Region (1) is thermal stress during substrate heating, region (2) is the growth stress due to Si<sub>3</sub>N<sub>4</sub> buried layer, region (3) is the growth of pure Pt thin films, region (4) is the stress relaxation of Pt after growth while holding at same temperature as it grew, region (4) is the thermal stress due to cooling.

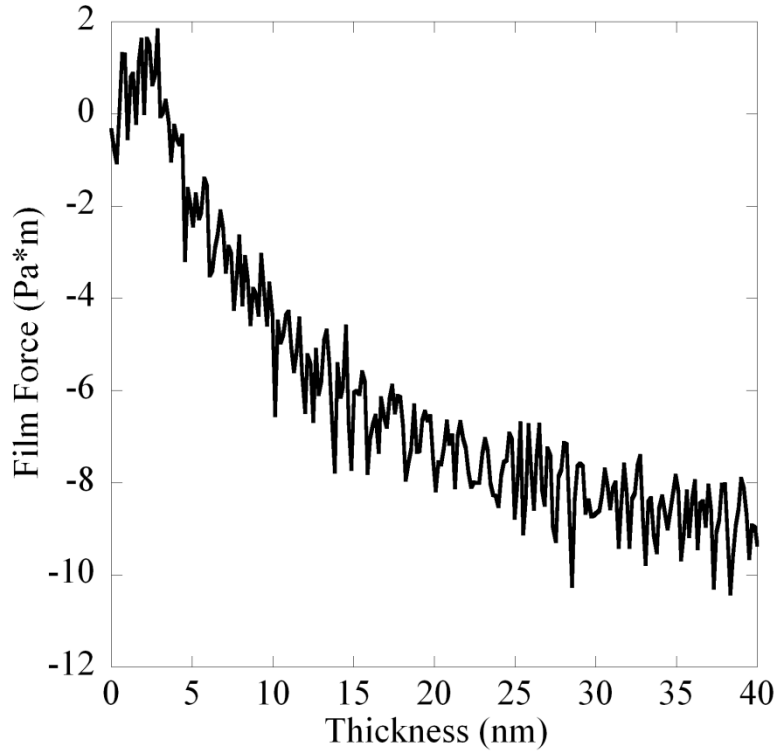


**Figure A.2:** The stress after the subtraction of the stress from the  $\text{Si}_3\text{N}_4$  buried layer and the thermal stress due to different thermal expansion coefficients of the substrate and the thin films. The region (3) in figure A.1 was plotted and showed the compressive-tensile-compressive evolution during the Pt thin film growth.

APPENDIX B

FePt and FeCu PHASE DIAGRAM

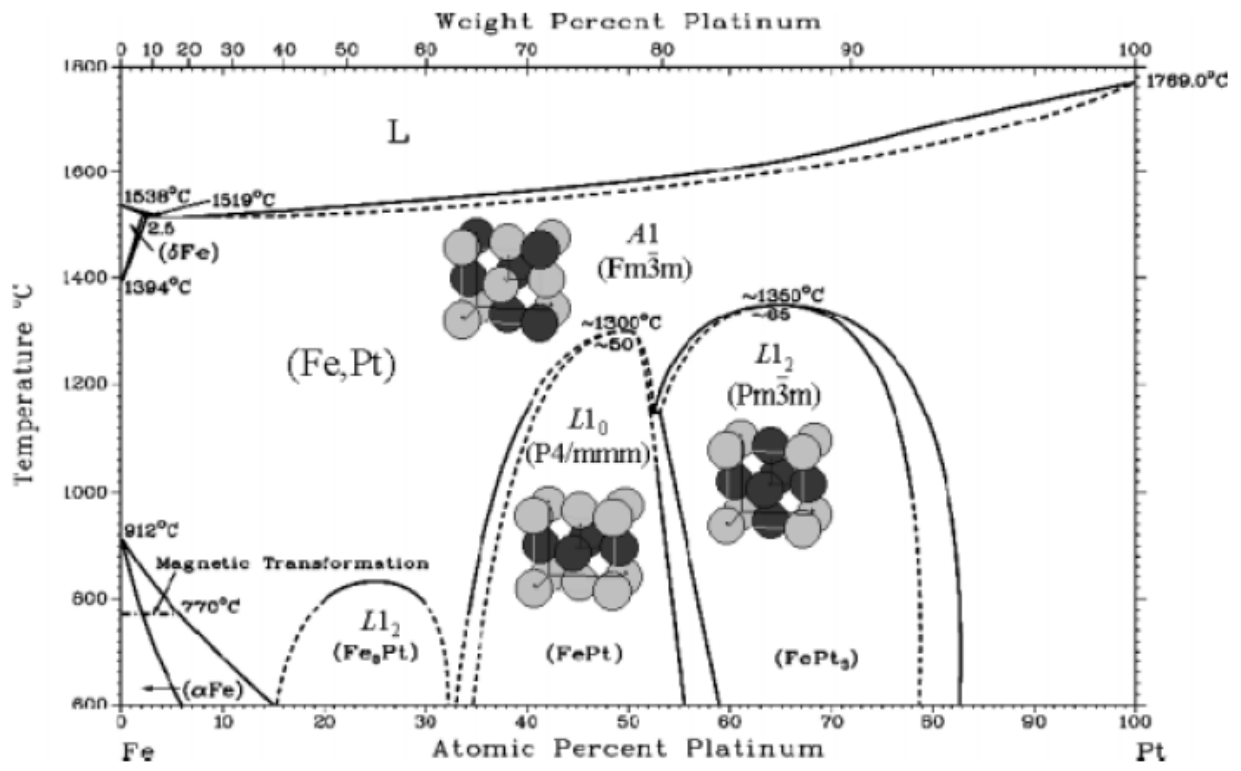


Figure B.1: Fe-Pt phase diagram, taken from [62].

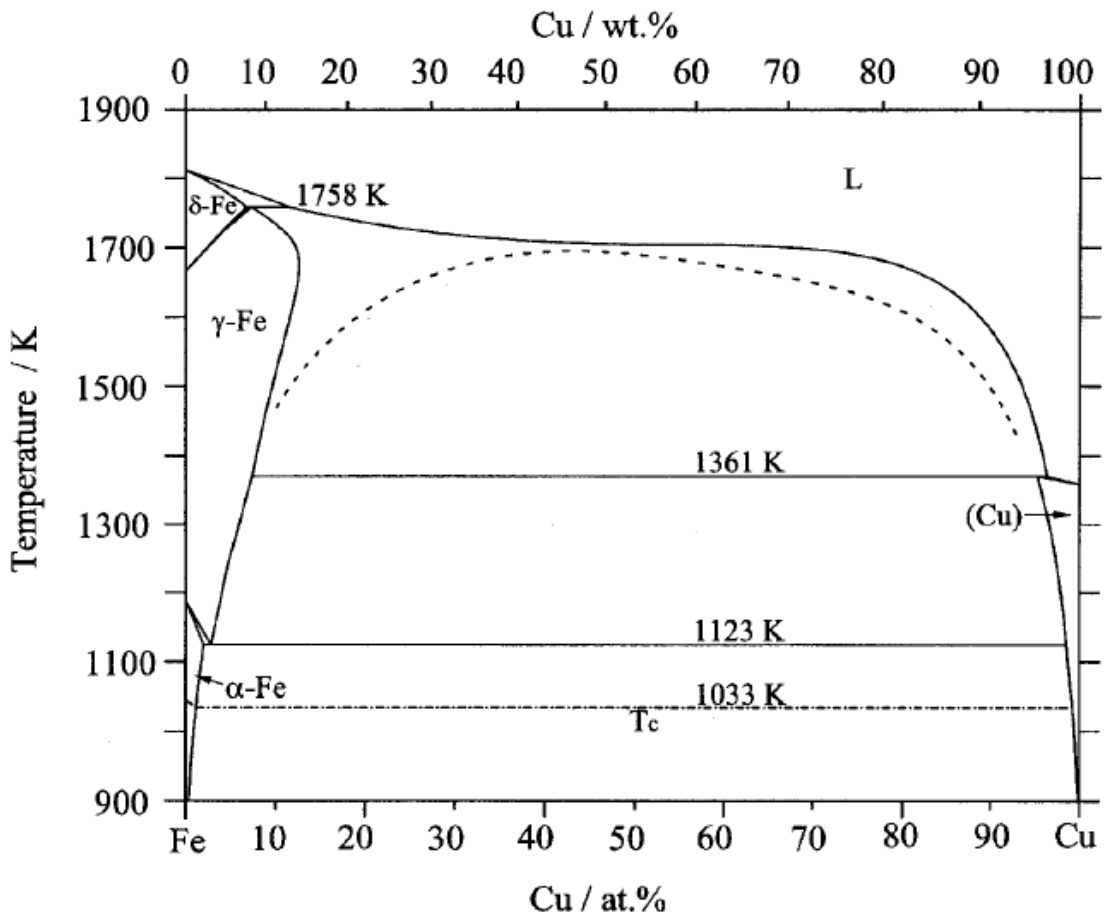


Figure B.2: FeCu phase diagram, taken from [63].